Eur. J. Mineral., 33, 727–742, 2021
https://doi.org/10.5194/ejm-33-727-2021

European Journal of Mineralogy
Open Access

Ellinaite, $CaCr_2O_4$, a new natural post-spinel oxide from Hatrurim Basin, Israel, and Juína kimberlite field, Brazil

Victor V. Sharygin[1,2], Sergey N. Britvin[3,4], Felix V. Kaminsky[5], Richard Wirth[6], Elena N. Nigmatulina[1], Grigory A. Yakovlev[2], Konstantin A. Novoselov[7], and Mikhail N. Murashko[3]

[1]V.S. Sobolev Institute of Geology and Mineralogy, Siberian Branch of the RAS, 3 prospekt Akad. Koptyuga, Novosibirsk 630090, Russia
[2]ExtraTerra Consortium, Institute of Physics and Technology, Ural Federal University, 21 Mira Str., Ekaterinburg 620002, Russia
[3]Institute of Earth Sciences, Saint Petersburg State University, 7/9 Universitetskaya Nab., St. Petersburg 199034, Russia
[4]Nanomaterials Research Center, Kola Science Center of the RAS, 14 Fersman Str., Apatity 184209, Russia
[5]V.I. Vernadsky Institute of Geochemistry and Analytical Chemistry, 19 Kosygin Str., Moscow 119334, Russia
[6]Helmholtz Centre Potsdam, GFZ German Research Centre for Geosciences, Section 3.3, Telegrafenberg, Potsdam 14473, Germany
[7]South Urals Federal Research Center of Mineralogy and Geoecology, Uralian Branch of the RAS, Miass 456317, Russia

Correspondence: Victor V. Sharygin (sharygin@igm.nsc.ru)

Received: 26 July 2021 – Accepted: 27 September 2021 – Published: 3 December 2021

Abstract. Ellinaite, a natural analog of the post-spinel phase β-$CaCr_2O_4$, was discovered at the Hatrurim Basin, Hatrurim pyrometamorphic formation (the Mottled Zone), Israel, and in an inclusion within the super-deep diamond collected at the placer of the Sorriso River, Juína kimberlite field, Brazil. Ellinaite at the Hatrurim Basin is confined to a reduced rankinite–gehlenite paralava, where it occurs as subhedral grains up to 30 µm in association with gehlenite, rankinite and pyrrhotite or forms the rims overgrowing zoned chromite–magnesiochromite. The empirical formula of the Hatrurim sample is $(Ca_{0.960}Fe^{2+}_{0.016}Na_{0.012}Mg_{0.003})_{0.992}(Cr_{1.731}V^{3+}_{0.183}Ti^{3+}_{0.068}Al_{0.023}Ti^{4+}_{0.003})_{2.008}O_4$. The mineral crystallizes in the orthorhombic system, space group *Pnma*, unit-cell parameters refined from X-ray single-crystal data: a 8.868(9), b 2.885(3), c 10.355(11) Å, V 264.9(5) Å^3 and $Z = 4$. The crystal structure of ellinaite from the Hatrurim Basin has been solved and refined to $R_1 = 0.0588$ based on 388 independent observed reflections. Ellinaite in the Juína diamond occurs within the micron-sized polyphase inclusion in association with ferropericlase, magnesioferrite, orthorhombic $MgCr_2O_4$, unidentified iron carbide and graphite. Its empirical formula is $Ca_{1.07}(Cr_{1.71}Fe^{3+}_{0.06}V_{0.06}Ti_{0.03}Al_{0.03}Mg_{0.02}Mn_{0.02})_{\Sigma 1.93}O_4$. The unit-cell parameters obtained from HRTEM data are as follows: space group *Pnma*, a 9.017, b 2.874 Å, c 10.170 Å, V 263.55 Å^3, $Z = 4$. Ellinaite belongs to a group of natural tunnel-structured oxides of the general formula AB_2O_4, the so-called post-spinel minerals: marokite $CaMn_2O_4$, xieite $FeCr_2O_4$, harmunite $CaFe_2O_4$, wernerkrauseite $CaFe^{3+}_2Mn^{4+}O_6$, chenmingite $FeCr_2O_4$, maohokite $MgFe_2O_4$ and tschaunerite $Fe(FeTi)O_4$. The mineral from both occurrences seems to be crystallized under highly reduced conditions at high temperatures (>1000 °C), but under different pressure: near-surface (Hatrurim Basin) and lower mantle (Juína diamond).

1 Introduction

The double oxide $CaCr_2O_4$ is known as an important component of composite materials explored in metallurgy and as ceramic materials (Róg et al., 2007). The α- and β-polymorphs of $CaCr_2O_4$, corresponding to its high- and low-temperature forms, demonstrate the promising magnetic and magnetoelectric properties (Hill et al., 1956; Pausch and Müller Buschbaum, 1974; Hörkner and Müller Buschbaum, 1976; Degterov and Pelton, 1996; Lee and Nassaralla, 1997; Damay et al., 2010; Toth et al., 2011; Zhai et al., 2016, and references herein). The β-polymorph belongs to a series of double oxides having the parent structure of $CaFe_2O_4$ (CF), which, altogether with $CaTi_2^{3+}O_4$ (CT) and $CaMn_2^{3+}O_4$ (CM), are gathered under the group name of *post-spinel phases* (Hill et al., 1956; Bright et al., 1958; Hörkner and Müller Buschbaum, 1976; Irifune et al., 1991; Kirby et al., 1996; Damay et al., 2010; Xue et al., 2021). These oxides are regarded as structural models for the high-pressure (HP) oxyspinels stable at the conditions of Earth's deep mantle (Chen et al., 2003a; Zhai et al., 2016, and references herein). Diverse synthetic compounds with post-spinel structure of the general formula AB_2O_4 are known, where *A* is Li, Na, Mg, Ca, Sr, Ba, La and Eu and *B* is Ti, V, Cr, Mn, Fe, Ru, Rh, Al, Ga, In, Tl, Sc, Y and REE (Shizuya et al., 2007).

In nature, seven post-spinel minerals were described prior to 2019: marokite $CaMn_2^{3+}O_4$ (Gaudefroy et al., 1963; Lepicard and Protas, 1966), xieite $FeCr_2^{3+}O_4$ (Chen et al., 2003a, b, 2008), harmunite $CaFe_2^{3+}O_4$ (Galuskina et al., 2014), wernerkrauseite $CaFe_2^{3+}Mn^{4+}O_6$ (Galuskin et al., 2016), chenmingite $FeCr_2^{3+}O_4$ (Chen et al., 2003b; Ma et al., 2019), maohokite $MgFe_2^{3+}O_4$ (Chen et al., 2019) and tschaunerite $Fe^{2+}(Fe^{2+}Ti^{4+})O_4$ (Ma and Prakapenka, 2018). Xieite, chenmingite, maohokite and tschaunerite are considered to be HP polymorphs, whereas other minerals may be formed under low-pressure conditions. Xieite, a HP polymorph of chromite $FeCr_2O_4$, was found in the shock veins of the Suizhou L6 meteorite, China (Chen et al., 2008), and maohokite, a HP polymorph of magnesioferrite, was reported in shocked gneiss from the Xiuyan crater in China (Chen et al., 2019). Chenmingite and tschaunerite were observed as shock-induced phases in the Tissint and Shergotty martian meteorites (Ma et al., 2019; Ma and Prakapenka, 2018). Harmunite $CaFe_2O_4$ and wernerkrauseite $CaFe_2^{3+}Mn^{4+}O_6$ are more common of Ca-rich high-temperature low-pressure pyrometamorphic rocks (Chesnokov et al., 1991; Nigmatulina, 2006; Nigmatulina and Nigmatulina, 2009; Galuskina et al., 2014; Sharygin, 2015; Galuskin et al., 2016). The Ca–Cr oxide phase, chemically and structurally similar to synthetic β-$CaCr_2O_4$, and post-spinel $(Mg,Mn)(Cr,Fe)_2O_4$ were found as potentially new mineral species in a microinclusion in a diamond from Brazil (Kaminsky et al., 2015). Unfortunately, the HRTEM data obtained and very small sizes were insufficient to approve these phases as new minerals.

This work covers all data obtained for a new mineral ellinaite, a natural analog of β-$CaCr_2O_4$, coming from two diverse localities: rankinite–gehlenite paralava at Hatrurim Basin, Hatrurim pyrometamorphic formation (Mottled Zone), Israel (holotype, Sharygin, 2019; Sharygin et al., 2019a), and a micron-sized inclusion in a diamond from the Sorriso River, Brazil (co-type; Kaminsky et al., 2015). The mineral was approved by the Commission on New Minerals, Nomenclature and Classification (CNMNC) of the International Mineralogical Association (IMA) as a new mineral species in December 2019, IMA 2019-091 (Sharygin et al., 2020). After the IMA registration, the same mineral has also been identified in varicolored spurrite marbles at Tulul Al Hammam, Daba-Siwaqa, Hatrurim pyrometamorphic formation, central Jordan (Galuskina et al., 2021a).

Ellinaite is named in honor of Ellina Vladimirovna Sokol (b. 1961) from IGM, Novosibirsk, Russia. Ellina (Ella) Sokol is a well-known Russian mineralogist and petrologist, who specialized in the studies of pyrometamorphic and combustion metamorphic rocks around the world, including the Hatrurim Formation (Mottled Zone) rocks, Israel–Jordan (Sokol et al., 2002, 2005, 2008, 2010, 2011, 2012, 2014a, b, 2015, 2017, 2019a, b, 2020; Khoury et al., 2016; Seryotkin et al., 2019; Sharygin et al., 2006, 2008, 2019b; Vapnik et al., 2007; Zateeva et al., 2007, and many other works).

An individual grain of ellinaite from rankinite–gehlenite paralava, Hatrurim Basin, Israel (sample MP-2013-6, used for many studies), was deposited in the collections of the A.E. Fersman Mineralogical Museum of the Russian Academy of Sciences, Moscow, Russia, with the registration number 5439/1 (holotype). Another grain of ellinaite from this Hatrurim paralava (in polished thin section) is in the collections of the Central Siberian Geological Museum at V.S. Sobolev Institute of Geology and Mineralogy (IGM), Siberian Branch of the RAS, Novosibirsk, Russia (catalogue number VII-102/1, holotype). The co-type sample of ellinaite from Córigo Sorriso, Mato Grosso State, Brazil (TEM foil from diamond), is located in the scientific collection of F.V. Kaminsky (V.I. Vernadsky Institute of Geochemistry and Analytical Chemistry, Moscow, Russia).

2 General data for ellinaite from Brazil

Natural ellinaite was first found in a polyphase inclusion within diamond #8-108 (foil #3601) (Kaminsky et al., 2015), collected from gravels of the Córigo Sorriso (Sorriso River, a right tributary of Rio Aripuanã), Juína kimberlite field, Mato Grosso State, Brazil (11°20′ S, 59°11′ W). It should be noted that the Juína kimberlite field is a well-known occurrence of the super-deep diamonds from both alluvial and primary kimberlite sources (Harte et al., 1999; Hutchison et al., 2001; Hayman et al., 2005; Kaminsky et al., 2001,

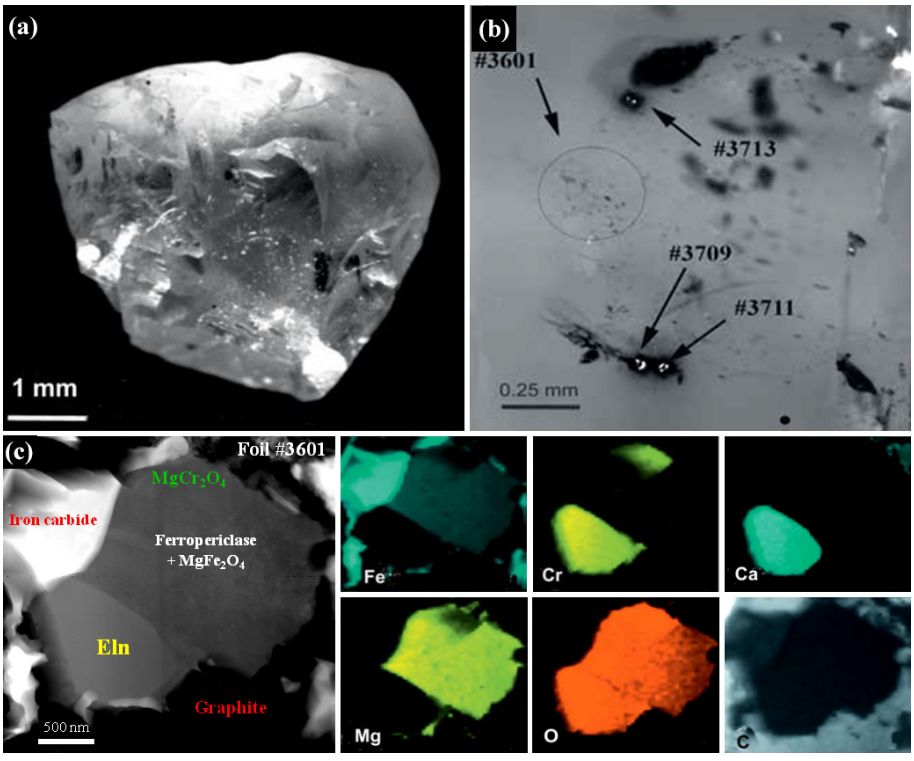

Figure 1. **(a)** General view of diamond #8-108, Brazil. **(b)** Positions of TEM foils in the diamond. **(c)** Polyphase mineral inclusion with ellinaite, foil #3601, TEM image and elemental maps. Symbols: Eln – ellinaite; $MgCr_2O_4$ – orthorhombic $MgCr_2O_4$; $MgFe_2O_4$ – magnesioferrite; Iron carbide – $Fe_2(C,N)$, $Fe_3(C,N)$ or $Fe_7(C,N)_3$. Data were adapted from Kaminsky et al. (2015).

2009, 2013, 2015; Walter et al., 2008; Bulanova et al., 2010, and references herein).

Unfortunately, no new data for ellinaite in the Brazilian diamond have been obtained since the IMA registration of this mineral (Sharygin et al., 2020). As a result, the text below and figures provided here for the Brazilian ellinaite represent a compilation of data adapted from Kaminsky et al. (2015).

Within the polyphase inclusion ellinaite is associated with ferropericlase (+magnesioferrite), orthorhombic $MgCr_2O_4$, iron carbide and graphite (Figs. 1 and S1 in the Supplement). It occurs as a 2×1 µm subhedral grain. The EDX TEM spectrum for ellinaite (Fig. S1) was obtained by applying the TIA™ software package and using the k_{AB} factors from the software. The quantitative results were normalized to the total sum of 100 %. The approximate uncertainties are ±3 % for concentrations in the range 30 at %–50 at %, ±6 %–12 % for concentrations between 5 at %–25 at %, ±12 %–25 % for concentrations between 1 at %–5 at % and ±25 %–100 % for concentrations below 1 at %. The composition (in at %, without oxygen) is Ca = 35.72, Cr = 57.02, Fe = 1.93, Mg = 0.79, Mn = 0.69, Al = 0.80, Ti = 1.09 and V = 1.96. The empirical formula calculated on the basis of three cations and four oxygens is $Ca_{1.07}(Cr_{1.71}Fe^{3+}_{0.06}V_{0.06}Ti_{0.03}Al_{0.03}Mg_{0.02}Mn_{0.02})_{\Sigma 1.93}O_4$.

The unit-cell parameters were calculated from HRTEM data (see Table 5 in Kaminsky et al., 2015) using high-resolution images and fast Fourier transform (FFT) software packages (Fig. S1) and gave the following results: orthorhombic symmetry, space group *Pnma* (#62), $a =$ 9.017 Å, $b = 2.874$ Å, $c = 10.170$ Å, $V = 263.55$ Å^3 and $Z = 4$.

3 Analytical methods for the Hatrurim Basin ellinaite

Double-polished sections (~ 50–100 µm in thickness) of the Hatrurim rankinite–gehlenite paralava (sample MP-2013-6, Fig. 2) were used for optical examination in transmitted and reflected light and for other studies.

Identification of ellinaite and related minerals in the Hatrurim rankinite–gehlenite paralavas was based on energy-dispersive spectra (EDS), back-scattered electron (BSE) images and elemental mapping (EDS system), using a TESCAN MIRA 3MLU scanning electron microscope equipped with an INCA Energy 450 XMax 80 microanalysis system (Oxford Instruments Ltd., Abingdon, UK) at the IGM, Novosibirsk, Russia. EDS analyses of minerals were operated at an accelerating voltage of 20 kV and a probe current of 1 nA in high-vacuum mode and at an accumulation time of 20–40 s. Synthetic compounds, pure metals and

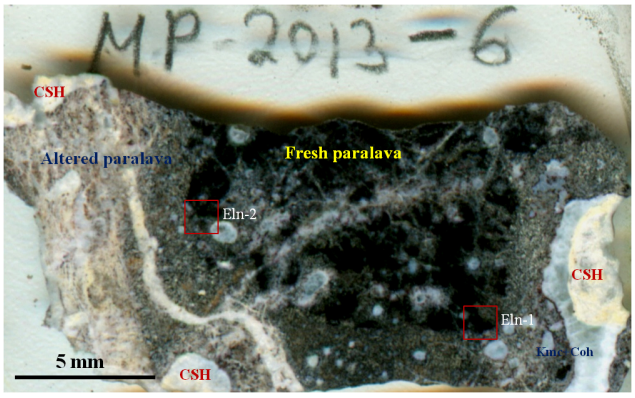

Figure 2. General view of gehlenite-rankinite paralava fragment, containing ellinaite (thin section, sample MP-2013-6). CSH – hydrated calcium silicates; Kmc+Coh – kamacite–cohenite association. Red squares – areas of individual grains of ellinaite (Eln-1 and Eln-2).

minerals were used as reference standards for the elements SiO_2 (Si and O), Al_2O_3 (Al), diopside (Mg and Ca), albite (Na), orthoclase (K), $Ca_2P_2O_7$ (P), BaF_2 (Ba and F), Cr_2O_3 (Cr), $CsRe_2Cl_6$ (Cl), $LaPO_4$ (La), $CePO_4$ (Ce), SrF_2 (Sr), metallic Nb, Ti, Ta, Zr, Fe, Mn, Zn and V. Matrix effects were corrected using the XPP algorithm, implemented in the software of the microanalysis system. Metallic Co served for quantitative optimization (normalization to probe current and energy calibration of the spectrometer).

Electron microprobe analyses (EMPA-WDS) of ellinaite and related minerals were done at the IGM, using a JEOL JXA-8100 electron microprobe (Jeol Ltd., Tokyo, Japan). Grains (sizes >5 µm) previously analyzed by EDS were selected for this purpose. Operating conditions were as follows: beam diameter of 1–2 µm, accelerating voltage of 20 kV and beam current of 15 nA, and counting time of 15 s (10 s – counting of backgrounds; 5 s – counting of peak for element). Pyrope (Si, Al, Mg, Fe), ilmenite (Ti), chromite (Cr), Sr-silicate glass (Sr), zircon (Zr), baryte (S), wollastonite (Ca), spessartine (Mn), albite (Na), chlorapatite (P, Cl), $NiFe_2O_4$ (Ni) and V_2O_5 (V) were used as standards during measuring. Precision of analysis for major elements was better than 2 % relative. Detection limits for elements were as follows (in parts per million, ppm): Si – 401, Ti – 182, Al – 303, Fe – 156, Mg – 309, Ca – 116, Cr – 192, Mn – 133, Sr – 766, Na – 239, K – 101, Cl – 98, Ni – 162 and S – 234. Data reduction was performed using a PAP routine (Pouchou and Pichoir, 1985). Overlap corrections were done for the following elements: Si$K\alpha$–Sr$L\alpha$, Ti$K\beta$–V$L\alpha$ and Cr$K\beta$–Mn$K\alpha$.

Reflectance data for ellinaite were obtained using a microscope spectrophotometer LOMO MSP-R equipped with spectrophotometric attachment PEI "R928" (Hamamatsu, Japan) at the South Urals Federal Research Center of Mineralogy and Geoecology, Miass, Russia. Measurements were done in the air using a ×40 objective with numerical aperture of 0.65: photometric diaphragm – 0.3 mm, size of analyzing area – 0.007 mm, diffraction grating – 600 grooves per millimeter, spectral interval – 6 nm, voltage for PEI – 450 V and standard – elemental silicon. Measurements were provided for the 400–700 nm range.

Single-crystal data were collected by means of a Bruker Kappa APEX DUO CCD diffractometer using Mo$K\alpha$ radiation. The crystal structure of ellinaite has been solved by the dual space method and refined to $R_1 = 0.059$ using the *SHELX*-2014 set of programs (Scheldrick, 2015) via the Olex2 v.1.2.8 graphical user interface (Dolomanov et al., 2009). Further details of data collection and structure refinement can be retrieved from the CIF attached to the Supplement.

The Raman spectra for ellinaite were recorded on a LabRAM HR 800 mm (HORIBA Scientific Ltd.) spectrometer equipped with a 1024 pixel LN/CCD detector and coupled to an Olympus BX40 confocal microscope (×100 objective) at the IGM. A semiconductor laser emitting at 514.5 nm with a nominal output power of 50 mW was used for excitation. In each case, 20 spectra were recorded for 20 s each at a hole diameter of 200 µm and a resolution of 0.5 cm^{-1} and then integrated. Most spectra were recorded between 100 and 1400 cm^{-1}. The monochromator was calibrated using the 520.7 cm^{-1} Raman line of elemental Si.

Electron backscatter diffraction (EBSD) studies were provided for one grain of ellinaite. The sample containing ellinaite and intended for EBSD studies was subjected to polishing by BuehlerMasterMet2 non-crystallizing colloidal silica suspension (0.02 µm). EBSD measurements were carried out by means of a FE-SEM ZEISS SIGMA VP scanning electron microscope equipped with an HKL Technology Nordlys HKL EBSD, operated at 20 kV and 1.4 nA in focused beam mode with a 70° tilted stage at the NANOTECH Center, Ural Federal University, Ekaterinburg, Russia. Structural identification of ellinaite was performed by matching its EBSD patterns with the reference structural models using the program FLAMENCO. The structural data for synthetic β-$CaCr_2O_4$ (Damay et al., 2010) and α-$CaCr_2O_4$ (Pausch and Müller Buschbaum, 1974) were used for the Kikuchi pattern simulation and comparison.

4 General information for ellinaite-bearing paralava at Hatrurim Basin, Israel

Ellinaite was observed in one of the rankinite–gehlenite paralavas, which were first found in 2011 in the southern part of the Hatrurim Basin, the largest combustion metamorphism complex of the Hatrurim Formation (also known as the "Mottled Zone") within Israel (Gross, 1977; Burg et al., 1992; Vapnik et al., 2007). The paralava with ellinaite (sample MP-2013-6) was found as a boulder in the dry Zohav wadi (nahal Zohav), near the Arad – Dead Sea

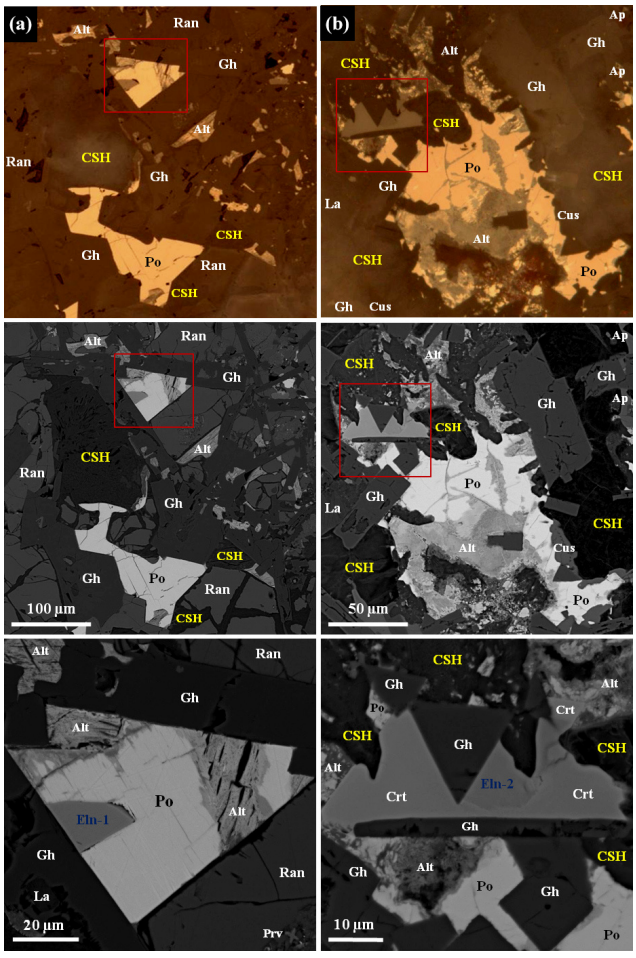

Figure 3. Areas with ellinaite in gehlenite-rankinite paralava **(a–b)**, Hatrurim Basin, Israel. BSE and reflected light images. Symbols: Eln-1, Eln-2 – ellinaite; Po – Cr-rich pyrrhotite; Gh – gehlenite; Ran – rankinite; La – larnite–flamite; Prv – Si-rich perovskite; Alt – alteration products after pyrrhotite; Ap – fluorapatite; Cus – cuspidine; Crt – chromite–magnesiochromite; CSH – hydrated calcium silicates. See Figs. 2, 4, S2 and S3 for details.

road (31°09′47″ N, 35°17′57″ E). Similar paralavas with abundant phosphides are also known in the midstream of the Halamish wadi (nahal Halamish, neighboring nahal Zohav) in the Hatrurim Basin (Britvin et al., 2015, 2017, 2019a–d, 2020a–c, 2021a. b).

The rock is moderately to highly weathered and brecciated and has the appearance of a "pseudoconglomerate", in which individual fragments are "cemented" and cross-cut by a carbonate–gypsum–Ca–hydrosilicate matrix. In general the individual fragments are altered in different degrees and contain abundant vesicles now partially filled with Ca hydrosilicates. The alteration degree is indicated by color change (from dark to white) from the center to rim (Fig. 2). The dark parts of some fragments are less weathered and consist of gehlenite, rankinite, larnite, flamite, cuspidine, Cr-rich pyrrhotite, fluorapatite and Si–Cr–V-rich perovskite as essential minerals. Minor and accessory phases are represented by chromite–magnesiochromite, wüstite–magnesiowüstite, wollastonite, Ti-rich cuspidine, ellinaite, Ba-rich djerfisherite minerals, magnetite, unidentified Ca–Fe silicate $Ca_4Fe_2(SiO_4)_3$ and oxysulfide close to $CaFe_3S_2O_5$, the $(Ni,Fe)_2As$ phase, pentlandite, native iron, cohenite, schreibersite Fe_3P, and barringerite Fe_2P (e.g., Britvin et al., 2015, 2017). Crystallization of the paralava likely occurred under highly reduced conditions that are determined by the chemistry of the essential minerals: Ca silicates and perovskite are very poor in Fe, whereas sulfides (pyrrhotite, Ba-rich phases), chromite, wüstite, native iron and phosphides are the main carriers of Fe. A list of mineral phases found in the rankinite–gehlenite paralava with ellinaite (sample MP-2013-6) and chemical composition of essential minerals are given in Tables S1 and S2. The metal-phosphide mineralization is mainly localized along the boundary of rock fragments with the carbonate–gypsum–Ca–hydrosilicate matrix, rarely around vesicles in the paralava. It forms rounded isolations varying in size from 10 µm to 1–2 mm and modal composition. Namely, in such associations the new phosphide minerals (murashkoite FeP, transjordanite Ni_2P, zuktamrurite FeP_2, negevite NiP_2, halamishite Ni_5P_4, polekhovskyite $MoNiP_2$, nazarovite $Ni_{12}P_5$) were first found in the Halamish wadi, Hatrurim Basin (Britvin et al., 2015, 2017, 2019a–d, 2020a–c). The following metal-phosphide assemblages with Cr–V-rich pyrrhotite are most common in the Zohav paralava: kamacite, steadite (Fe–P eutectics, mainly kamacite + schreibersite Fe_3P) + kamacite, barringerite Fe_2P + steadite, schreibersite + barringerite, barringerite + murashkoite and murashkoite + transjordanite. Other phosphide phases, cohenite, graphite, copper, Mo-rich phases, unidentified phosphates and daubreelite sometimes occur in such assemblages. The formation of paralava and metal-phosphide mineralization appears to be unrelated in that the metal-phosphide assemblage was probably formed in the solidified paralava from reduced gases (Britvin et al., 2015, 2017, 2019a–d). In addition to the metal phosphide and sulfide association, the new Fe–Ni-rich phosphates were found in the carbonate–gypsum–Ca–hydrosilicate matrix as alteration products of phosphides (phosphocyclite-(Fe) $Fe_2^{2+}(P_4O_{12})$ (IMA 2020-087), phosphocyclite-(Ni) $Ni_2^{2+}(P_4O_{12})$ (IMA 2020-088), beershevaite $CaFe_3^{3+}(PO_4)_3O$ (IMA 2020-095a), lisanite $CaNi^{2+}P_2O_7$ (IMA 2021-014), shasuite $CaNi_3^{2+}(P_2O_7)_2$ (IMA 2021-20), nabateaite $Fe_2^{2+}(P_2O_7)$ (IMA 2021-26) and samraite $Ni_2^{2+}(P_2O_7)$ (IMA 2021-29)) in the Halamish rocks (Britvin et al., 2021a).

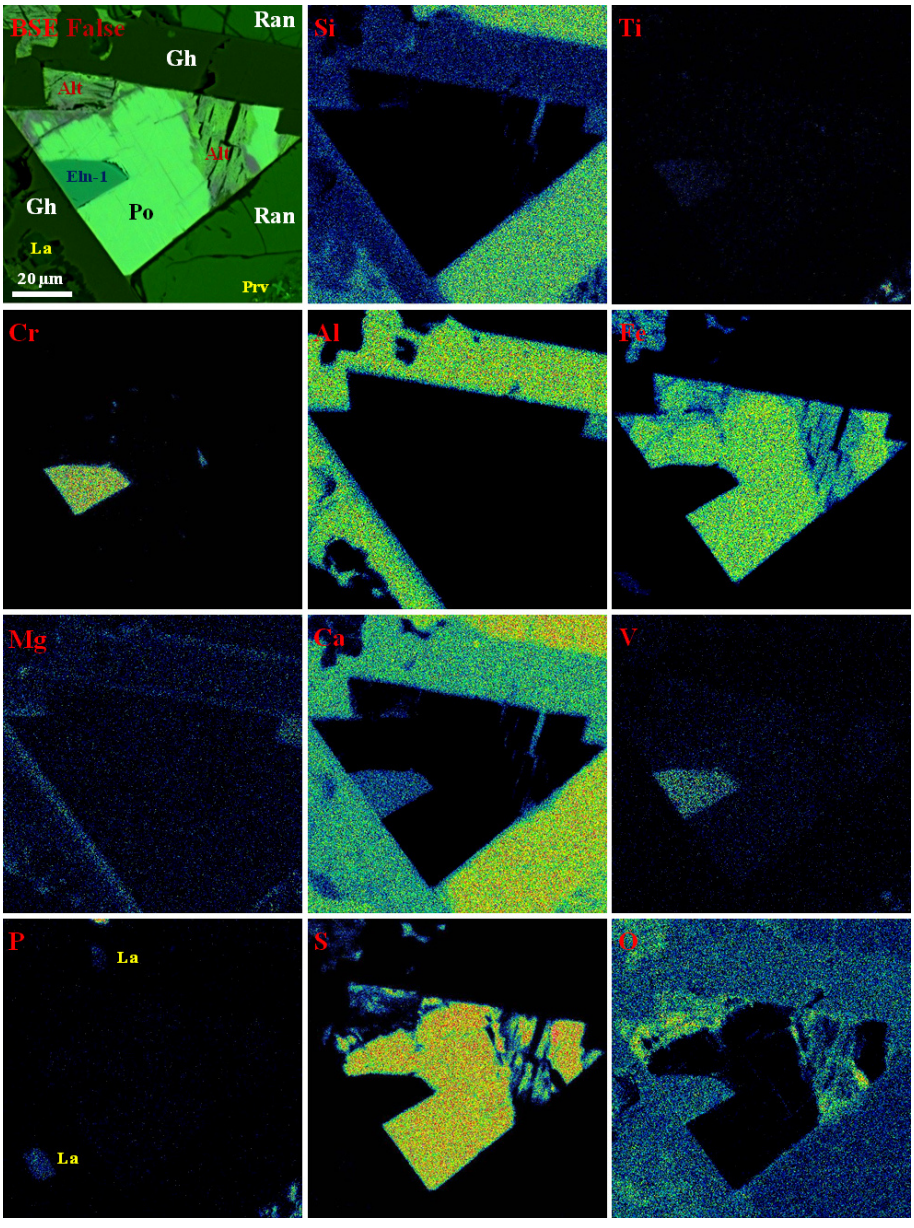

Figure 4. Elemental maps of mineral association with ellinaite-1 grain from gehlenite-rankinite paralava, Hatrurim Basin, Israel. Symbols: Eln-1 – ellinaite; Po – Cr-rich pyrrhotite; Gh – gehlenite; Ran – rankinite; La – larnite–flamite; Prv – Si-rich perovskite; Alt – alteration products after pyrrhotite. See Figs. 3a and S2 for details.

5 Morphology and optical and physical properties of ellinaite from Hatrurim Basin

Ellinaite is very rare mineral in the Hatrurim Basin, and only two grains were observed in a dark unaltered part of the rankinite–gehlenite paralava (Fig. 2). It forms subhedral opaque grains in association with gehlenite, rankinite and pyrrhotite (size – 30×20 µm, ellinaite-1 grain, Figs. 3a, 4 and S2) or is intergrown with chromite–magnesiochromite (size – 10×10 µm, ellinaite-2 grain, Figs. 3b and S3). In reflected light and in BSE images this phase resembles perovskite and chromite, which are more abundant in the studied paralava. Mineral relations indicate that ellinaite crystallized after gehlenite, rankinite and chromite, but before pyrrhotite (Fig. 3).

The color of ellinaite is black, and the color of the powdered mineral is black. It is brittle and has submetallic luster. Its hardness is ≈ 4.5–5 (Mohs), which is close to neighboring chromite (Fig. 3b). No cleavage and parting were observed; fracture is uneven. Microhardness and density were not measured directly because of the small grain size of ellinaite. Density calculated from unit-cell

Table 1. Reflectance values for ellinaite from Hatrurim Basin, Israel.

λ (nm)	R_{max}	R_{min}	λ (nm)	R_{max}	R_{min}
400	17.19	16.85	560	14.63	14.51
420	16.55	16.25	580	14.56	14.45
440	16.26	16.00	**589**	**14.55**	**14.42**
460	15.82	15.56	600	14.51	14.41
470	**15.63**	**15.35**	620	14.54	14.42
480	15.45	15.17	640	14.57	14.43
500	15.12	14.94	**650**	**14.54**	**14.48**
520	14.89	14.76	660	14.69	14.52
540	14.75	14.62	680	14.80	14.59
546	**14.73**	**14.59**	700	14.95	14.70

The ellinaite-1 grain was used for measurements. Bold – interpolated values.

dimensions and results of electron-microprobe analyses is 5.217 g cm^{-3}. Ellinaite is weakly distinguishable optically from the black chromite–magnesiochromite in reflected light and in BSE images (Figs. 3b and S3). Under reflected light it is gray with a blue tint and shows weak red-brown internal reflections. Bireflectance and pleochroism are not observed; anisotropy is weak. The reflectance data for the mineral in air are given in Table 1. Reflectance percentages for the four R_{max} and R_{min} COM (Commission on Ore Mineralogy) wavelengths are 15.63, 15.35 (470 nm); 14.73, 14.59 (546 nm); 14.55, 14.42 (589 nm); and 14.54, 14.48 (650 nm).

6 Chemical composition of the holotype specimen (Hatrurim Basin)

The empirical formula of ellinaite calculated on the basis of three cations and four oxygens and WDS-EDS data ($n = 48$) is $(Ca_{0.960}Fe^{2+}_{0.016}Na_{0.012}Mg_{0.003})_{0.992}(Cr_{1.731}V^{3+}_{0.183}Ti^{3+}_{0.068}Al_{0.023}Ti^{4+}_{0.003})_{2.008}O_4$. The average data for two ellinaite grains are given in Table 2, and the database for the Hatrurim Basin ellinaite is represented in Tables S3 and S4 (Supplement). Taking into account the reduced conditions for paralava crystallization (presence of native iron, cohenite and Cr-rich pyrrhotite) and excess of positive charge in a calculated formula, a dominant three-valence state is suggested for Ti. Thus, the simplified formula for the Hatrurim ellinaite may be expressed as $Ca(Cr^{3+},V^{3+},Ti^{3+})_2O_4$ and the ideal formula as $CaCr_2O_4$, which requires (in wt %) CaO 26.95, Cr_2O_3 73.05 and total 100.00. Alternatively, a formula version with minor vacancy at the Ca site and tetravalent Ti may also be considered. In this case the empirical formula (on the basis of four oxygens) is $(Ca_{0.952}Fe^{2+}_{0.016}Na_{0.012}Mg_{0.003})_{0.983}(Cr_{1.716}V^{3+}_{0.182}Ti^{4+}_{0.071}Al_{0.023})_{1.991}O_4$.

The main variation (4 wt %–7 wt %) of the Hatrurim ellinaite composition is in the amounts of TiO_2, V_2O_3 and Cr_2O_3 (Fig. 5). Both ellinaite grains are drastically different in composition (Table 1): $(Ca_{0.964}Fe^{2+}_{0.017}Na_{0.011})_{0.992}(Cr_{1.702}V^{3+}_{0.198}Ti^{3+}_{0.079}Al_{0.025}Ti^{4+}_{0.004})_{2.008}O_4$ (ellinaite-1) and $(Ca_{0.946}Fe^{2+}_{0.017}Na_{0.014}Mg_{0.012})_{0.989}(Cr_{1.841}V^{3+}_{0.127}Ti^{3+}_{0.026}Al_{0.014}Ti^{4+}_{0.003})_{2.011}O_4$ (ellinaite-2). The variations within individual grains are not very significant (Fig. 5) and may indicate a slight chemical heterogeneity like that of core-to-rim variation. It should be noted that such inhomogeneous distribution is weakly highlighted in elemental maps (Figs. 4, S2 and S3). For example, the Ti-richest (TiO_2 total – 4.7 wt %) and V-richest (V_2O_3 – 8.1 wt %) compositions within the ellinaite-1 grain are $(Ca_{0.960}Fe^{2+}_{0.020}Na_{0.009}Mn_{0.001}Mg_{0.001})_{0.991}(Cr_{1.653}V^{3+}_{0.206}Ti^{3+}_{0.122}Al_{0.028})_{2.009}O_4$ and $(Ca_{0.975}Fe^{2+}_{0.013}Na_{0.006})_{0.994}(Cr_{1.686}V^{3+}_{0.224}Ti^{3+}_{0.073}Al_{0.023})_{2.006}O_4$ (Table S3). Negative correlations of Cr with Ti and V (Fig. 5) strongly suggest the occurrence of limited isomorphous substitutions according to possible schemes: $Cr^{3+} \leftrightarrow (V^{3+},Ti^{3+})$ and

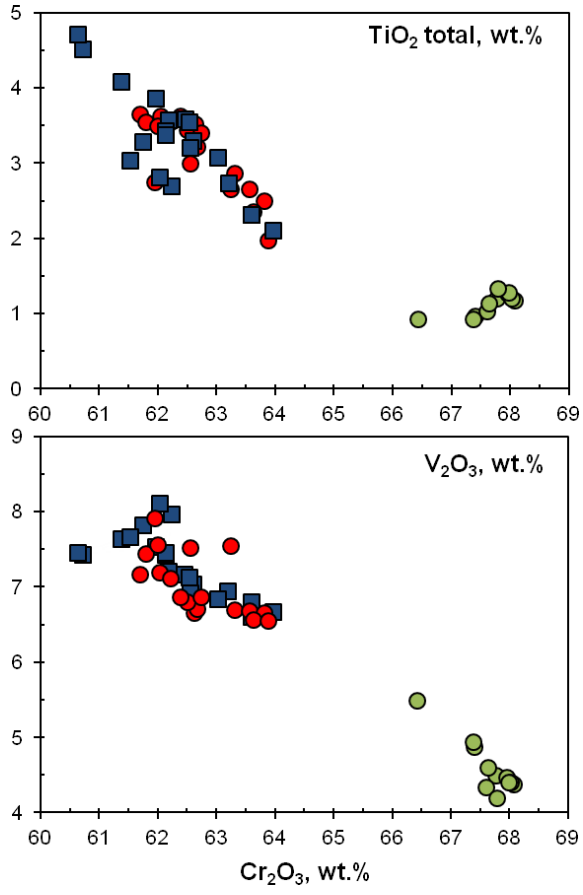

Figure 5. Chemical variations (in wt %) of TiO_2 and V_2O_3 versus Cr_2O_3 in ellinaite from the Hatrurim Basin. Ellinaite-1 grain: blue squares – WDS data; red circles – EDS data. Green circles – EDS data for the ellinaite-2 grain. For the database for the Hatrurim Basin ellinaite, see Tables S3 and S4.

Table 2. Chemical composition (in wt %) for ellinaite from rankinite–gehlenite paralava (sample MP-2013-6), Hatrurim Basin, in comparison with ellinaite from the Daba-Siwaqa spurrite marble and the Brazilian diamond and ideal composition $CaCr_2O_4$.

	Ellinaite-1				Ellinaite-2				Ellinaite	Ellinaite	Ideal
Locality	Hatrurim Basin, Israel				Hatrurim Basin, Israel				Daba-Siwaqa, Jordan	Sorriso River, Brazil	
	$n = 38$	SD	Min	Max	$n = 10$	SD	Min	Max	$n = 10$	$n = 1$	
TiO_2	0.14	0.19	0.00	0.53	0.12	0.14	0.00	0.47	1.27	1.17	
Ti_2O_3	2.75	0.71	1.47	4.23	0.91	0.23	0.42	1.12			
Cr_2O_3	62.50	0.82	60.64	63.97	67.64	0.49	66.43	68.07	65.44	63.27	73.05
V_2O_3	7.17	0.44	6.55	8.11	4.59	0.39	4.19	5.49		2.19	
Al_2O_3	0.62	0.10	0.40	0.89	0.35	0.07	0.26	0.47	1.71	0.74	
Fe_2O_3									1.43	2.33	
FeO	0.56	0.12	0.37	0.88	0.59	0.22	0.30	0.85			
MnO	0.01	0.01	0.00	0.04	0.01	0.03	0.00	0.09		0.69	
MgO	0.00	0.01	0.00	0.03	0.23	0.18	0.00	0.50	0.62	0.39	
CaO	26.13	0.17	25.87	26.51	25.65	0.44	25.08	26.23	27.95	29.21	26.95
SrO									0.54		
Na_2O	0.17	0.05	0.07	0.31	0.21	0.03	0.00	0.25			
Sum	100.04				100.30				98.96	100.00	100.00
Formula based on three cations and four oxygens											
Ti^{4+}	0.004				0.003				0.033	0.030	
Ti^{3+}	0.079				0.026						
Cr	1.702				1.841				1.785	1.710	2.000
V^{3+}	0.198				0.127					0.060	
Al	0.025				0.014				0.070	0.030	
Fe^{3+}									0.037	0.060	
Sum	2.008				2.011				1.924	1.890	2.000
Fe^{2+}	0.016				0.017						
Mn	0.000				0.000					0.020	
Mg	0.000				0.012				0.032	0.020	
Ca	0.964				0.946				1.033	1.070	1.000
Sr									0.011		
Na	0.011				0.014						
Sum	0.992				0.989				1.076	1.110	1.000

For Hatrurim Basin, SiO_2, NiO and SrO are below detection limits (<0.005 wt %). Formula based on three cations and four oxygens. Ti_2O_3 and TiO_2 is calculated by charge balance. Ellinaite-1 – WDS + EDS data; Ellinaite-2 – EDS data. The database for the Hatrurim Basin ellinaite is given in Tables S3 and S4. Composition of ellinaite in the Brazilian diamond (Kaminsky et al., 2015) are recalculated in wt % of oxides. Data for ellinaite at Tulul Al Hammam, Daba-Siwaqa, Jordan, are quoted from Galuskina et al. (2021a).

$2Cr^{3+} \leftrightarrow V^{3+} + Ti^{3+}$. Unfortunately, we have no possibility to check the valence state of Ti and other elements due to the small amount of ellinaite present.

Ellinaite from the Hatrurim Basin paralava essentially differs in composition from the same mineral in the Brazilian diamond, $Ca_{1.07}(Cr_{1.71}Fe^{3+}_{0.06}V_{0.06}Ti^{4+}_{0.03}Al_{0.03}Mg_{0.02}Mn_{0.02})_{\Sigma 1.93}O_4$ (Kaminsky et al., 2015), and in the Jordanian spurrite marble, $(Ca_{1.033}Mg_{0.032}Sr_{0.011})_{1.076}(Cr_{1.785}Fe^{3+}_{0.037}Ti^{4+}_{0.033}Al_{0.070})_{\Sigma 1.924}O_4$ (Galuskina et al., 2021a). The Hatrurim ellinaite has higher concentrations of Ti (dominantly Ti^{3+}) and V and a lower amount of Fe (dominantly Fe^{2+}) compared with the other two occurrences. The Brazilian and Jordanian ellinaites are characterized by a high concentration of Fe^{3+} and low content of total Ti^{4+}. In the Brazilian sample the valence state of Fe (as Fe^{3+}) in ellinaite is anomalous considering the presence of associated Fe carbide and ferropericlase in the diamond-hosted inclusion (Kaminsky et al., 2015). In the Jordanian case we do not see any contradictions since Fe-oxide minerals (brownmillerite, srebrodolskite, hematite) and garnet-supergroup minerals (mainly andradite and priscillagrewite-(Y)) in spurrite marble are dominated by Fe^{3+} (Galuskina et al., 2021a, b).

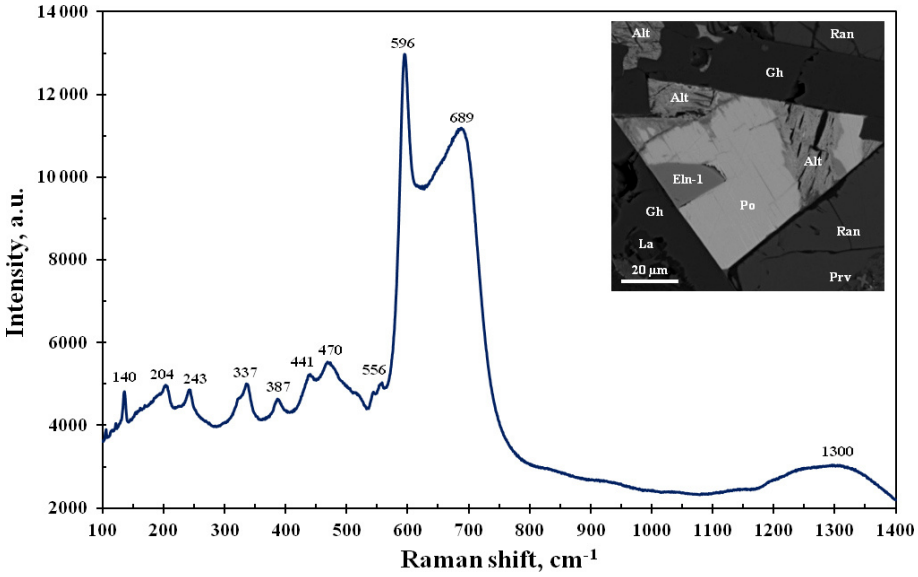

Figure 6. BSE image and Raman spectrum for ellinaite from the Hatrurim Basin, Israel (see also Fig. 3). Symbols: Eln-1 – ellinaite-1 grain; Po – Cr-rich pyrrhotite; Gh – gehlenite; Ran – rankinite; La – larnite; Prv – Si-rich perovskite; Alt – alteration products after pyrrhotite.

7 Structural data for ellinaite from Hatrurim Basin

7.1 Raman spectroscopy

The Raman spectra for the Hatrurim ellinaite show the complete band set common to synthetic β-$CaCr_2O_4$ (Zhai et al., 2016). However, in addition to the strong 596 cm^{-1} band, the Hatrurim phase indicates the strong and broad band at 690 cm^{-1} with respect to the synthetic compound (Fig. 6). This seems to be related to crystallographic orientation of the natural sample. The appearance and disappearance of some bands and their shifting and intensity change in the dependency on orientation have been shown for the Raman spectra of synthetic $CaFe_2O_4$ (Kolev et al., 2003). The vibration modes of the Raman spectrum of ellinaite may be interpreted by analogy with the Raman spectra of harmunite and wernerkrauseite and related synthetic compounds (Kolev et al., 2003; Galuskina et al., 2014; Galuskin et al., 2016; Zhai et al., 2016). Observed Raman bands are (cm^{-1}) $\sim$ 1300 (combination first-order phonons A_g in the 680–700 range); 689, 598 and 556 (A_g – stretching modes); 470 and 441 (B_{2g} and A_g – tilting and bending modes); 387, 337 and 324 (A_g, B_{1g} and B_{3g} – rotating modes); 243 and 204 (A_g); 140 (A_g and B_{2g}); and 123 and 107 (A_g) (Ca-related vibrations). In general, Raman spectra of ellinaite from Hatrurim Basin are similar to those of ellinaite from Jordan (Galuskina et al., 2021a).

7.2 EBSD study

Before single-crystal X-ray study, we attempted to obtain the EBSD data for ellinaite. Two structural patterns of synthetic $CaCr_2O_4$ were used for EBSD comparison studies: α-$CaCr_2O_4$ (Toth et al., 2011) and β-$CaCr_2O_4$ (Damay et al., 2010). We determined a good diffraction pattern, but, unfortunately, it was not indexed in both comparison structural models. This appears to have been due to unsuccessful orientation of the ellinaite crystal, although the data obtained indicated an orthorhombic symmetry. The forced Kikuchi pattern using the β-$CaCr_2O_4$ model (Damay et al., 2010) outlined strong mean angular deviation for some diffraction lines (Fig. S4).

7.3 X-ray data for ellinaite

Single-crystal X-ray studies for the Hatrurim ellinaite indicate that ellinaite is related to the orthorhombic crystal system: space group *Pnma* (#62), $a = 8.868(9)$ Å, $b = 2.885(3)$ Å, $c = 10.355(11)$ Å, $V = 264.9(5)$ Å^3 and $Z = 4$. X-ray powder diffraction data could not be obtained because of scarcity of material. Powder diffraction pattern calculated on the basis of single-crystal structural data and chemical composition is given in Table 3. Data were calculated using the STOE WinXPOW v.2.02 software (Stoe & Cie, 2006).

7.4 Crystal structure of ellinaite

The crystal structure of ellinaite has been solved by the dual space method and refined to $R_1 = 0.059$ using the *SHELX*-2014 set of programs (Scheldrick, 2015) via Olex2 v.1.2.8 graphical user interface (Dolomanov et al., 2009). The data collection and structure refinement details are summarized in Table 4. Fractional atomic coordinates, displacement parameters and selected bond lengths for the crystal structure of ellinaite are given in Tables 5 and 6.

Table 3. Calculated X-ray powder diffraction pattern (d in angstroms) for ellinaite from the Hatrurim Basin.

I_{calc}	d_{calc}	hkl	I_{calc}	d_{calc}	hkl
3	5.1774	002	2	1.6940	106
6	4.4712	102	6	1.6824	015
23	4.4341	200	3	1.6779	502
15	3.3678	202	4	1.6646	412
2	3.2166	103	15	1.6083	206
4	2.8425	301	3	1.5664	413
9	2.7791	011	10	1.4904	306
2	2.7237	203	9	1.4780	600
6	2.6519	111	1	1.4632	601
54	2.5887	004	2	1.4631	504
100	2.5671	302	1	1.4621	315
4	2.4850	104	14	1.4608	116
69	2.4241	112	1	1.4591	107
32	2.4181	210	**20**	1.4543	414
1	2.2452	303	12	1.4504	512
1	2.2356	204	17	1.4425	020
6	2.2135	013	1	1.4212	602
3	2.1909	212	9	1.4047	216
3	2.1679	401	1	1.4032	207
34	2.1476	113	1	1.3717	220
11	2.0380	402	3	1.3618	406
16	2.0248	311	1	1.3587	603
3	2.0167	105	1	1.3259	222
2	1.9805	213	2	1.3241	316
5	1.9178	312	1	1.3154	610
15	1.8828	114	1	1.3020	117
2	1.8764	205	1	1.2944	008
9	1.7718	313	6	1.2835	604
35	1.7671	214	3	1.2808	108
22	1.7579	410	1	1.2749	612
1	1.7482	501	1	1.2619	217
14	1.7331	411	6	1.2600	024
1	1.7258	006	13	1.2575	322
1	1.6961	305			

The ellinaite-1 grain was used. The nine strongest lines are in bold. Data were calculated using the STOE WinXPOW v.2.02 software (Stoe & Cie, 2006).

In general, the crystal structure of ellinaite may be represented as a framework built up of two types of the distorted $[Cr^{3+}O_6]$ octahedra (Cr1 and Cr2), sharing common edges and corners and containing the system of channels (tunnels) propagated along the b axis. The channels are occupied by calcium ions (Fig. 7). The framework is composed of two types of the distorted $[Cr^{3+}O_6]$ octahedra (Cr1 and Cr2), which form double chains, connected by common oxygen corners. The distorted octahedra $[Cr^{3+}O_6]$ in the chains have different average distances: Cr1–O = 1.950(3) Å and Cr2–O = 1.962(9) Å (Table 6). Owing to the specific connection of the chains, each tunnel has a cross section of a distorted trigonal prism (Fig. 7).

Table 4. Crystal parameters, data collection and structure refinement details for the holotype ellinaite (Hatrurim Basin, Israel).

Crystal data	
Formula	$CaCr_2O_4$
Crystal size (mm)	$0.03 \times 0.02 \times 0.02$
Crystal system	Orthorhombic
Space group	*Pnma*
a (Å)	8.868(9)
b (Å)	2.885(3)
c (Å)	10.355(11)
V (Å^3)	264.9(5)
Z	4
D_x (g cm^{-3})	5.217
Data collection and refinement	
Radiation	Mo$K\alpha$ ($\lambda = 0.71073$ Å)
Temperature (K)	293
2Θ range (°)	6.00–54.00
Total reflections collected	2189
No. of unique reflections	348
No. of unique observed, $I \geq 2\sigma(I)$	312
h, k, l range	$-11 \rightarrow 11$, $-3 \rightarrow 3$, $-13 \rightarrow 13$
$F(000)$	400
μ (mm^{-1})	9.94
No. of refined parameters	43
$R_{int.}$	0.080
R_σ	0.031
R_1 [$F \geq 4\sigma(F)$]	0.059
R_1 (all data)	0.063
wR_2	0.1459
S = GoF	1.105

The ellinaite-1 crystal was used.

8 Discussion and final remarks

Ellinaite is related to multiple oxides with the general formula AB_2O_4. However, ellinaite does not belong to the spinel subgroup of the spinel supergroup (Biagioni and Pasero, 2014; Bosi et al., 2019) because it has a tunnel structure (post-spinel structure). Currently, minerals with this structure are regarded as belonging to the hypothetical marokite subgroup, which now includes eight minerals: marokite $CaMn_2^{3+}O_4$ (Gaudefroy et al., 1963; Lepicard and Protas, 1966), xieite $FeCr_2^{3+}O_4$ (Chen et al., 2003a, b, 2008), harmunite $CaFe_2^{3+}O_4$ (Galuskina et al., 2014), wernerkrauseite $CaFe_2^{3+}Mn^{4+}O_6$ (Galuskin et al., 2016), chenmingite $FeCr_2^{3+}O_4$ (Chen et al., 2003b; Ma et al., 2018), maohokite $MgFe_2^{3+}O_4$ (Chen et al., 2019), tschaunerite $Fe^{2+}(Fe^{2+}Ti^{4+})O_4$ (Ma and Prakapenka, 2018) and ellinaite $CaCr_2O_4$ (this work). Comparative crystallographic data for these minerals are given in Table 7. Moreover, the orthorhombic $MgCr_2O_4$ phase ($a = 9.467$ Å, $b = 2.905$ Å, $c = 9.550$ Å), which is associated with ellinaite in the Brazilian diamond-hosted inclusion (Kaminsky et al., 2015), appears to be related to the marokite supergroup. This phase may be considered a Mg analog of chenmingite $FeCr_2O_4$ observed as a shock-induced phase in the Tissint martian

Table 5. Fractional atomic coordinates and displacement parameters (Å^2) for ellinaite (Hatrurim Basin).

Site*	x/a	y/b	z/c	U_{iso}	U^{11}	U^{22}	U^{33}	U^{13}
Ca1 (4*c*)	0.2589(2)	3/4	0.34162(17)	0.0222(7)	0.0220(10)	0.0315(11)	0.0133(11)	−0.0007(6)
Cr1 (4*c*)	0.41706(16)	3/4	0.60142(13)	0.0160(6)	0.0181(9)	0.0209(9)	0.0091(9)	−0.0002(4)
Cr2 (4*c*)	0.56064(17)	1/4	0.88744(13)	0.0163(6)	0.0196(9)	0.0200(9)	0.0094(9)	0.0001(4)
O1 (4*c*)	0.4729(6)	1/4	0.7152(5)	0.0160(12)	0.021(3)	0.020(3)	0.006(2)	0.002(2)
O2 (4*c*)	0.5828(6)	1/4	0.0733(6)	0.0179(13)	0.018(3)	0.027(3)	0.010(3)	0.001(2)
O3 (4*c*)	0.7043(7)	3/4	0.8416(5)	0.0165(12)	0.017(3)	0.021(3)	0.012(3)	0.001(2)
O4 (4*c*)	0.3837(6)	1/4	0.4759(5)	0.0170(12)	0.020(3)	0.021(3)	0.010(3)	0.004(2)

* Site multiplicities and Wyckoff symbols are given in parentheses. U^{12} and U^{23} are equal to zero by default.

Table 6. Selected bond lengths (Å) for ellinaite (Hatrurim Basin).

Bond	Length	Bond	Length	Bond	Length
Ca1–O1	2.450(6)	Cr1–O1	1.927(4) × 2	Cr2–O1	1.946(6)
Ca1–O1	2.438(6)	Cr1–O3	1.977(7)	Cr2–O2	1.935(7)
Ca1–O2	2.301(5) × 2	Cr1–O4	1.964(4)	Cr2–O2	1.965(4) × 2
Ca1–O3	2.405(5) × 2	Cr1–O4	1.940(6)	Cr2–O3	1.982(4) × 2
Ca1–O4	2.289(5) × 2	Cr1–O4	1.964(4)		

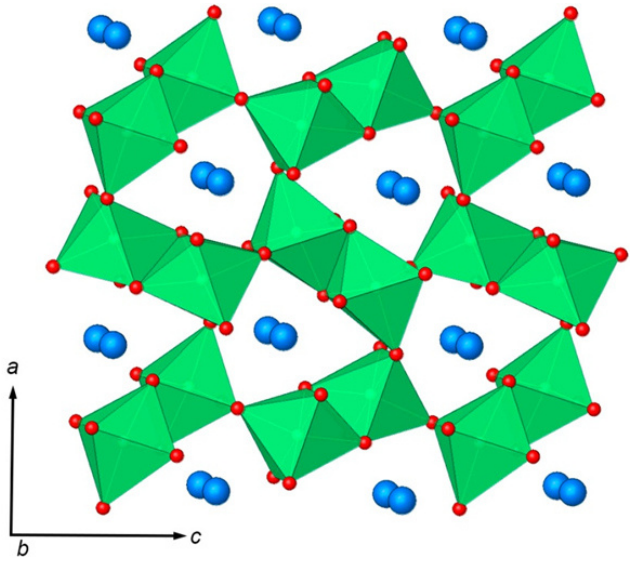

Figure 7. The crystal structure of ellinaite. A framework composed of edge- and corner-sharing [CrO_6] octahedra (green) contains the system of channels propagated along the *b* axis. The channels are occupied by calcium ions (blue spheres).

meteorite (Chen et al., 2003b; Ma et al., 2019) or xieite $FeCr_2O_4$ found in the shock veins of the Suizhou L6 meteorite (Chen et al., 2003a, b, 2008).

Initially high content of Cr in the sedimentary protolith (100–480 ppm Cr) was favorable to high abundance of Cr in the Hatrurim Basin pyrometamorphic rocks (100–800 ppm Cr) and then the appearance of Cr-rich minerals in them (Geller et al., 2012; Seryotkin et al., 2019; Sokol et al., 2019a). In the rankinite–gehlenite paralava this is fixed in the presence of Cr-dominant oxides (chromite – 62.2 wt %–64.3 wt % Cr_2O_3, magnesiochromite – 61.3 wt %–62.3 wt % Cr_2O_3, ellinaite – 60.6 wt %–68.6 wt % Cr_2O_3) and Cr-containing oxides (Si-rich perovskite – 1.6 wt %–2.8 wt % Cr_2O_3, magnetite – up to 3.0 wt % Cr_2O_3) and sulfides (pyrrhotite – 0.0 wt %–2.4 wt % Cr, Ba–Cr sulfide – 21.7 wt %–26.7 wt % Cr) (Tables 1 and S2). Like ellinaite, chromite, magnesiochromite and perovskite are also enriched in V_2O_3 – 7.4 wt %–8.6 wt %, 3.3 wt %–3.9 wt % and 1.5 wt %–1.9 wt %, respectively (Tables 1 and S2). In contrast to the above minerals Ca silicates and fluorapatite in the paralava are virtually free in these oxides (Table S2). It should also be mentioned that varicolored spurrite marbles at Tulul Al Hammam, central Jordan (third occurrence of ellinaite), are also characterized by high concentrations of Cr (40–1880 ppm Cr; Sokol et al., 2020), and in addition to ellinaite these rocks contain mcconnelite $CuCrO_2$, zincochromite and magnesiochromite (Galuskina et al., 2021a, b). In general, all types of pyrometamorphic rocks of the Hatrurim Formation (Israel–Jordan) have a remarkably high concentration of Cr (Gross, 1977; Sharygin et al., 2008; Sokol et al., 2011, 2014a, b, 2019a, 2020; Geller et al., 2012; Seryotkin et al., 2019; Galuskina et al., 2021a, b).

The overview of ellinaite from the three localities assumes different PT–X–fO_2 conditions for the mineral and its host rocks. The structural data for ellinaite strongly indicate the β-$CaCr_2O_4$ modification and no evidence of the precursor α-$CaCr_2O_4$. According to the phase diagram CaO-Cr_2O_3 (Degterov and Pelton, 1996; Shabanova et al., 2019),

Table 7. Comparative crystallographic data for ellinaite and related post-spinel minerals.

Mineral	Formula	Structure type	Space group	a (Å)	b (Å)	c (Å)	V (Å^3)	Z	Reference
Ellinaite	$CaCr_2^{3+}O_4$	CF	*Pnma*	8.868	2.885	10.355	264.9	4	Holotype, Hatrurim Basin, Israel (this work)
	$CaCr_2^{3+}O_4$	CF	*Pnma*	9.017	2.874	10.17	263.55	4	Co-type, Córigo Sorriso, Brazil (Kaminsky et al., 2015)
	$CaCr_2^{3+}O_4$	CF	*Pnma*	9.0875	2.9698	10.6270	286.80	4	Daba-Siwaqa, Jordan (Galuskina et al., 2021a).
Marokite	$CaMn_2^{3+}O_4$	CM	*Pbcm**	9.71	3.162	10.03	307.76	4	Gaudefroy et al. (1963); Lepicard and Protas (1966)
Xieite	$FeCr_2^{3+}O_4$	CT	*Cmcm**	9.462	2.916	9.562	263.8	4	Chen et al. (2003a, b, 2008)
Harmunite	$CaFe_2^{3+}O_4$	CF	*Pnma*	9.2183	3.0175	10.6934	297.45	4	Galuskina et al. (2014)
Wernerkrauseite	$CaFe_2^{3+}Mn^{4+}O_6$	CF	*Pnma*	9.0548	2.8718	10.9908	285.8	8/3	Galuskin et al. (2016)
Maohokite	$MgFe_2^{3+}O_4$	CF	*Pnma*	8.907	9.937	2.981	263.85	4	Chen et al. (2019)
Chenmingite	$FeCr_2^{3+}O_4$	CF	*Pnma*	9.715	2.87	9.49	264.6	4	Chen et al. (2003b); Ma et al. (2019)
Tschaunerite	$Fe^{2+}(Fe^{2+}Ti^{4+})O_4$	CT	*Cmcm**	9.216	2.71	9.103	227.35	4	Ma and Prakapenka (2018)

Tunnel structures: CF – $CaFe_2^{3+}O_4$; CT – $CaTi_2^{3+}O_4$; CM – $CaMn_2^{3+}O_4$. * Transformed to standard setting.

the phase transition between α-$CaCr_2O_4$ and β-$CaCr_2O_4$ (ellinaite) is near 1600 °C (Fig. S5). The mineralogy of the diamond-hosted inclusion with ellinaite from Brazil (Fig. 1) indicates lower-mantle crystallization conditions and low fO_2 due to the presence of iron carbide and/or carbonitride (Kaminsky et al., 2015). Ellinaite-containing rocks of the Hatrurim Formation are characterized by near-surface pressure conditions and different T-fO_2 (this work; Galuskina et al., 2021a, b). Mineral relations in the Hatrurim Basin rankinite–gehlenite paralava indicate that gehlenite, rankinite and larnite are the earliest phases crystallizing from Ca-rich silicate paralava melt (Fig. 3). Other minerals occupy interstitial spaces between the above phases and were clearly formed after them. Ellinaite crystallized after chromite but before pyrrhotite. According to experimental and calculated data for the system $CaO–SiO_2–Al_2O_3$ (Mao et al., 2006; Haccuria et al., 2015), gehlenite+rankinite+larnite is the liquidus association (peritectic) at 1317–1343 °C, and rankinite occupies a very narrow field at temperatures near 1308 °C. The formation of pyrrhotite as the latest phase was probably near 1000 °C according to Kosyakov et al. (1996). Silicate-melt inclusions in schorlomite–rankinite–melilite paralava from the Hatrurim Basin indicate that rankinite crystallized at $T > 1160$ °C (Sharygin et al., 2006).

The presence of Cr-rich pyrrhotite, wüstite, native iron, cohenite and phosphides (Table S1) in the Hatrurim rankinite–gehlenite paralava indicates highly reduced conditions. Thus, local melting of the calcareous sedimentary protolith, and crystallization of resultant rankinite–gehlenite paralava under reduced conditions with the formation of holotype ellinaite, is suggested to have occurred between 1000–1343 °C.

With respect to the ellinaite-bearing marbles in the Tulul Al Hammam area of Jordan, the presence of spurrite and calcite implies maximum metamorphic temperatures for these rocks of <950 °C (Sokol et al., 2005); Khoury et al. (2016) and Sokol et al. (2020) have subsequently determined values of 800–850 °C. On the other hand, Galuskina et al. (2021a, b) consider a value of ∼ 1000 °C as the maximum temperature for the ellinaite-bearing marbles and suggest the possibility that these rocks may be retrograde products of earlier pyrometamorphic crystallization with the formation of high-temperature Ca silicates and lime. The crystallization of the Tulul Al Hammam spurrite marbles with ellinaite occurred under oxidized conditions as evidenced by the presence of Fe-rich minerals (brownmillerite, srebrodolskite, hematite, andradite and priscillagrewite-(Y)), in which iron is largely present as Fe^{3+} (Galuskina et al., 2021a, b).

The compositional and structural data of ellinaite from three known localities show that it is stable under a wide range of PT–X–fO_2 conditions, i.e., from the Earth's surface to the lower mantle. Limited solid solutions in ellinaite such as $CaCr_2^{3+}O_4$ (ellinaite) ↔ $CaFe_2^{3+}O_4$ (harmunite), $CaCr_2^{3+}O_4 \leftrightarrow CaV_2^{3+}O_4$ and $CaCr_2^{3+}O_4 \leftrightarrow CaTi_2^{3+}O_4$ involving reduced and oxidized elements reflect variable redox environments, in which ellinaite formed.

Data availability. Crystallographic data for ellinaite (CIF) are available in the Supplement. This part also additionally contains four tables (Tables S1 to S4) and five figures (Figs. S1 to S5).

Supplement. The supplement related to this article is available online at: https://doi.org/10.5194/ejm-33-727-2021-supplement.

Author contributions. VVS provided Raman spectroscopy and SEM and microprobe analysis for the Hatrurim ellinaite and wrote the paper, with help from all coauthors. SNB performed single-crystal X-ray studies and refinement of the crystal structure for the Hatrurim ellinaite. FVK and RW conducted HRTEM and interpreted the results for the Brazilian ellinaite. ENN provided microprobe analyses and their complete processing for the Hatrurim ellinaite. GAY helped with EBSD study of the Hatrurim ellinaite. KAN identified optical properties of ellinaite. MNM provided fieldwork and collected phosphide-containing rocks at Hatrurim Basin, Israel.

Competing interests. The contact author has declared that neither they nor their co-authors have any competing interests.

Disclaimer. Publisher's note: Copernicus Publications remains neutral with regard to jurisdictional claims in published maps and institutional affiliations.

Acknowledgements. Victor V. Sharygin would like to thank Mikhail V. Khlestov and Nikolai S. Karmanov (IGM, Novosibirsk, Russia) for their technical assistance during SEM studies. Special thanks for Yevgeny Vapnik (Ben-Gurion University, Israel) for providing field trips at Hatrurim Basin (Israel). The authors are grateful to the Centre for X-ray diffraction studies at the St. Petersburg State University for the access to instrumental and computational resources. We are highly appreciative of the comments, suggestions and careful editing of reviewers (Rodney Grapes, Nikita V. Chukanov).

Financial support. Raman spectroscopy and EBSD investigations for the Hatrurim ellinaite were done on state assignment of IGM SB RAS (IX.125.2) and the Initiative Project of Ministry of Science and Higher Education of the Russian Federation (Act 211 of the Government of the Russian Federation (grant agreement no. 02.A03.21.0006)). SEM and microprobe studies for the Hatrurim ellinaite were supported by the Russian Science Foundation (grant no. 17-17-01056p). Crystallographic studies of the Hatrurim ellinaite were provided by the Russian Science Foundation (grant no. 18-17-00079).

Review statement. This paper was edited by Cristiano Ferraris and reviewed by Rodney Grapes and Nikita V. Chukanov.

References

Biagioni, C. and Pasero, M.: The systematics of the spinel-type minerals: an overview, Am. Mineral., 99, 1254–1264, https://doi.org/10.2138/am.2014.4816, 2014.

Bosi, F., Biagioni, C., and Pasero, M.: Nomenclature and classification of the spinel supergroup, Eur. J. Mineral., 31, 183–192, https://doi.org/10.1127/ejm/2019/0031-2788, 2019.

Bright, N. F. H., Rowland, J. F., and Wurm, J. G.: The compound $CaO.Ti_2O_3$, Can. J. Chem., 36, 492–495, https://doi.org/10.1139/v58-070, 1958.

Britvin, S. N., Murasko, M. N., Vapnik, Y., Polekhovsky, Y. S., and Krivovichev, S. V.: Earth's phosphides in Levant and insights into the source of Archaean prebiotic phosphorus, Sci. Rep., 5, 8355, https://doi.org/10.1038/srep08355, 2015.

Britvin, S. N., Murasko, M. N., Vapnik, E., Polekhovsky, Y. S., and Krivovichev, S. V.: Barringerite Fe_2P from pyrometamorphic rocks of the Hatrurim Formation, Israel, Geol. Ore Deposit, 59, 619–625, https://doi.org/10.1134/S1075701517070029, 2017.

Britvin, S. N., Murashko, M. N., Krzhizhanovskaya, M. G., Vereshchagin, O. S., Vapnik, Y., Shilovskikh, V. V., and Lozhkin, M. S.: Nazarovite, IMA 2019-013, CNMNC Newsletter No. 50, August 2019, Mineral. Mag., 83, 615–620, https://doi.org/10.1180/mgm.2019.46, 2019a.

Britvin, S. N., Murashko, M. N., Vapnik, Y., Polekhovsky, Y. S., Krivovichev, S. V., Vereshchagin, O. S., Vlasenko, N. S., Shilovskikh, V. V., and Zaitsev, A. N.: Zuktamrurite, FeP_2, a new mineral, the phosphide analogue of löllingite, $FeAs_2$, Phys. Chem. Mineral., 46, 361–369, https://doi.org/10.1007/s00269-018-1008-4, 2019b.

Britvin, S. N., Murashko, M. N., Vereshchagin, O. S., Vapnik, Y., Shilovskikh, V. V., and Vlasenko, N. S.: Polekhovskyite, IMA 2018-147, CNMNC Newsletter No. 48, April 2019, page 401, Eur. J. Mineral., 31, 399–402, 2019c.

Britvin, S. N., Vapnik, Y., Polekhovsky, Y.S., Krivovichev, S. V., Krzhizhanovskaya, M. G., Gorelova, L. A., Vereshchagin, O. S., Shilovskikh, V. V., and Zaitsev, A. N.: Murashkoite, FeP, a new terrestrial phosphide from pyrometamorphic rocks of the Hatrurim Formation, South Levant, Mineral. Petrol., 113, 237–248, https://doi.org/10.1007/s00710-018-0647-y, 2019d.

Britvin, S. N., Murashko, M. N., Vapnik, Y., Polekhovsky, Y. S., Krivovichev, S. V., Vereshchagin, O. S., Shilovskikh, V. V., and Krzhizhanovskaya, M. G.: Negevite, the pyrite-type NiP_2, a new terrestrial phosphide, Am. Mineral., 105, 422–427, https://doi.org/10.2138/am-2020-7192, 2020a.

Britvin, S. N., Murashko, M. N., Vapnik, Y., Polekhovsky, Y. S., Krivovichev, S. V., Krzhizhanovskaya, M. G., Vereshchagin, O. S., Shilovskikh, V. V., and Vlasenko, N. S.: Transjordanite, Ni_2P, a new terrestrial and meteoritic phosphide, and natural solid solutions barringerite-transjordanite (hexagonal Fe_2P-Ni_2P), Am. Mineral., 105, 428–436, https://doi.org/10.2138/am-2020-7275, 2020b.

Britvin, S. N., Murashko, M. N., Vapnik, Y., Polekhovsky, Y. S., Krivovichev, S. V., Vereshchagin, O. S., Shilovskikh, V. V., Vlasenko, N. S., and Krzhizhanovskaya, M. G.: Halamishite, Ni_5P_4, a new terrestrial phosphide in the Ni–P system, Phys. Chem. Mineral., 47, 3, https://doi.org/10.1007/s00269-019-01073-7, 2020c.

Britvin, S. N., Murashko, M. N., Vapnik, Y., Vlasenko, N. S., Krzhizhanovskaya, M. G., Vereshchagin, O. S., Bocharov,

V. N., and Lozhkin, M. S.: Cyclophosphates, a new class of native phosphorus compounds, and some insights into prebiotic phosphorylation on early Earth, Geology, 49, 382–386, https://doi.org/10.1130/G48203.1, 2021a.

Britvin, S. N., Vereshchagin, O. S., Shilovskikh, V. V., Krzhizhanovskaya, M. G., Gorelova, L. A., Vlasenko, N. S., Pakhomova, A. S., Zaitsev, A. N., Zolotarev, A. A., Bykov, M., and Nestola, F.: Discovery of terrestrial allabogdanite $(Fe,Ni)_2P$, and the effect of Ni and Mo substitution on the barringerite-allabogdanite high-pressure transition, Am. Mineral., 106, 944–952, https://doi.org/10.2138/am-2021-7621, 2021b.

Bulanova, G. P., Walter, M. J., Smith, C. B., Kohn, S. C., Armstrong, L. S., Blundy, J., and Gobbo, L.: Mineral inclusions in sublithospheric diamonds from Collier 4 kimberlite pipe, Juína, Brazil: subducted protoliths, carbonated melts and primary kimberlite magmatism, Contrib. Mineral. Petrol., 160, 489–510, https://doi.org/10.1007/s00410-010-0490-6, 2010.

Burg, A., Starinsky, A., Bartov, Y., and Kolodny, Y.: Geology of the Hatrurim Formation ("Mottled Zone") in the Hatrurim basin, Israel J. Earth Sci., 40, 107–124, 1992.

Chen, M., Shu, J., Mao, H.-K., Xie, X., and Hemley, R. J.: Natural occurrence and synthesis of two new postspinel polymorphs of chromite, P. Natl. Acad. Sci. USA, 100, 14651–14654, https://doi.org/10.1073/pnas.2136599100, 2003a.

Chen, M., Shu, J., Xie, X., and Mao, H.-K.: Natural $CaTi_2O_4$-structured $FeCr_2O_4$ polymorph in the Suizhou meteorite and its significance in mantle mineralogy, Geochim. Cosmochim. Ac., 67, 3937–3942, https://doi.org/10.1016/S0016-7037(03)00175-3, 2003b.

Chen, M., Shu, J., and Mao, H.-K.: Xieite, a new mineral of high-pressure $FeCr_2O_4$ polymorph, Chinese Sci. Bull., 53, 3341–3345, 2008.

Chen, M., Shu, J., Xie, X., and Tan, D.: Maohokite, a post-spinel polymorph of $MgFe_2O_4$ in shocked gneiss from the Xiuyan crater in China, Meteor. Planet. Sci., 54, 495–502, https://doi.org/10.1111/maps.13222, 2019.

Chesnokov, B. V., Bazhenova, L. F., Bushmakin, A. F., Vilisov, A. F., Lotova, E. V., Mikhal', T. A., Nishanbaev, T. P., and Shcherbakova, E. P.: New minerals from burnt dumps of the Chelyabinsk coal basin (the 2nd report), in: New Data on the Mineralogy of Endogenic Deposits and Technogenic Zones of the Urals, edited by: Chesnokov, B. V., PH UrD AS USSR, Sverdlovsk, USSR, 5–14, 1991 (in Russian).

Damay, F., Martin, C., Hardy, V., Maignan, A., Andre, G., Knight, K., Giblin S. R., and Chapon, L. C.: Zigzag ladders with staggered magnetic chirality in the $S = 3/2$ compound β-$CaCr_2O_4$, Phys. Rev. B, 81, 214405, https://doi.org/10.1103/PhysRevB.81.214405, 2010.

Degterov, S. and Pelton, A. D.: Critical evaluation and optimization of the thermodynamic properties and phase diagrams of the CrO-Cr_2O_3, CrO-Cr_2O_3-Al_2O_3, and CrO-Cr_2O_3-CaO systems, J. Phase Equilib., 17, 476–487, 1996.

Dolomanov, O. V., Bourhis, L. J., Gildea, R. J., Howard, J. A. and Puschmann, H.: *OLEX2*: a complete structure solution, refinement and analysis program, J. Appl. Crystallogr., 42, 339–341, https://doi.org/10.1107/S0021889808042726, 2009.

Galuskin, E. V., Kruger, B., Kruger, H., Blass, G., Widmer, R., and Galuskina, I. O.: Wernerkrauseite, $CaFe_2^{3+}Mn^{4+}O_6$: the first nonstoichiometric post-spinel mineral, from Bellerberg volcano, Eifel, Germany, Eur. J. Mineral., 28, 485–493, https://doi.org/10.1127/ejm/2016/0028-2509, 2016.

Galuskina, I. O., Vapnik, Y., Lazic, B., Armbruster, T., Murashko, M., and Galuskin, E. V.: Harmunite $CaFe_2O_4$: A new mineral from the Jabel Harmun, West Bank, Palestinian Autonomy, Israel, Am. Mineral., 99, 965–975, https://doi.org/10.2138/am.2014.4563, 2014.

Galuskina, I. O., Vapnik, Y., Stachowicz, M., Woźniak K., and Galuskin, E. V.: Mcconnellite, $CuCrO_2$, and ellinaite, $CaCr_2O_4$, from varicolored spurrite marble of the Daba-Siwaqa area, Hatrurim Complex, Jordan, Min. Mag., 85, 387–397, https://doi.org/10.1180/mgm.2021.27, 2021a.

Galuskina, I., Galuskin, E., Vapnik, Y., Zeliński, G., and Prusik, K.: Priscillagrewite-(Y), $(Ca_2Y)Zr_2Al_3O_{12}$ – a new garnet of the bitikleite group from the Daba-Siwaqa area, the Hatrurim Complex, Jordan, Am. Mineral., 106, 641–649, https://doi.org/10.2138/am-2021-7692, 2021b.

Gaudefroy, C., Jouravsky, G., and Permingeat, F.: La marokite, $CaMn_2O_4$ une nouvelle espèce minérale, B. Soc. Fr. Mineral. Cr., 86, 359–367, 1963.

Geller, Y.I., Burg, A., Halicz, L., and Kolodny, Y.: System closure during the combustion metamorphic "Mottled Zone" event, Israel. Chem. Geol., 334, 25–36, https://doi.org/10.1016/j.chemgeo.2012.09.029, 2012.

Gross, S.: The mineralogy of the Hatrurim Formation, Israel. Bull. Geol. Surv. Israel, 70, 1–80, 1977.

Haccuria, E., Crivits, T., Hayes, P. C., and Jak, E.: Selected phase equilibria studies in the Al_2O_3-CaO-SiO_2 system, J. Am. Ceram. Soc., 99, 691–704, https://doi.org/10.1111/jace.13991, 2015.

Harte, B., Harris, J. W., Hutchison, M. T., Watt, G. R., and Wilding, M. C.: Lower mantle mineral associations in diamonds from Sao Luiz, Brazil, in: Mantle petrology: field observations and high pressure experimentation, edited by: Fei, Y., Bertka, C. M., and Mysen, B. O., Geochemical Society Special Publications, Washington, USA, 125–153, 1999.

Hayman, P. C., Kopylova, M. G., and Kaminsky, F. V.: Lower mantle diamonds from Rio Soriso (Juína area, Mato Grosso, Brazil), Contrib. Mineral. Petrol., 140, 734–753, https://doi.org/10.1007/s00410-005-0657-8, 2005.

Hill, P. M., Peiser, H. S., and Rait, J. R.: The crystal structure of calcium ferrite and β calcium chromite, Acta Crystallogr., 9, 981–986, 1956.

Hörkner, W. and Müller-Buschbaum, H. K.: Einkristalluntersuchungen von β-$CaCr_2O_4$, Z. Naturforsch. B, 31, 1710–1711, 1976.

Hutchison, M. T., Hursthouse, M. B., and Light, M. E.: Mineral inclusions in diamonds: associations and chemical distinctions around the 670-km discontinuity, Contrib. Mineral. Petrol., 142, 119–126, https://doi.org/10.1007/s004100100279, 2001.

Irifune, T., Fujino, K., and Ohtani, K.: A new high pressure form of $MgAl_2O_4$, Nature, 349, 409–411, https://doi.org/10.1038/349409a0, 1991.

Kaminsky, F. V., Zakharchenko, O. D., Davies, R., Griffin, W. L., Khachatryan-Blinova, G. K., and Shiryaev, A. A.: Superdeep diamonds from the Juína area, Mato Grosso State, Brazil, Contrib. Mineral. Petrol., 140, 734–753, https://doi.org/10.1007/s004100000221, 2001.

Kaminsky, F. V., Khachatryan, G. K., Andreazza, P., Araujo, D. P., and Griffin, W. L.: Super-deep diamonds from kimberlites in

the Juína area, Mato Grosso State, Brazil, Lithos, 112, 833–842, https://doi.org/10.1016/J.LITHOS.2009.03.036, 2009.

Kaminsky, F. V., Wirth, R., and Schreiber, A.: Carbonatitic inclusions in deep mantle diamond from Juína, Brazil: New minerals in the carbonate-halide association, Can. Mineral., 51, 669–688, https://doi.org/10.3749/canmin.51.5.669, 2013.

Kaminsky, F., Wirth, R., and Schreiber, A.: A microinclusion of lower mantle rock and other mineral and nitrogen lower-mantle inclusions in a diamond, Can. Mineral., 53, 83–104, https://doi.org/10.3749/canmin.1400070, 2015.

Khoury, H. N., Sokol, E. V., Kokh, S. N., Seryotkin, Y. V., Nigmatulina, E. N., Goryainov, S. V., Belogub, E. V., and Clark, I. D.: Tululite, $Ca_{14}(Fe^{3+},Al)$ $(Al,Zn,Fe^{3+},Si,P,Mn,Mg)_{15}O_{36}$: A new Ca zincate-aluminate from combustion metamorphic marbles, central Jordan, Mineral. Petrol., 110, 125–140, https://doi.org/10.1007/s00710-015-0413-3, 2016.

Kirby, S. H., Stein, S., Okai, E. A., and Rubie, D. C.: Metastable mantle phase transformations and deep earthquakes in subducting oceanic lithosphere, Rev. Geophys., 34, 261–306, 1996.

Kolev, N., Iliev, M. N., Popov, V. N., and Gospodinov, M.: Temperature-dependent polarized Raman spectra of $CaFe_2O_4$, Solid State Comm., 128, 153–155, https://doi.org/10.1016/S0038-1098(03)00660-4, 2003.

Kosyakov, V. I., Kraeva, A. G., Fedorova, Z. N., and Sinyakova, E. F.: Topological analysis of evolution of phase equilibria in the Fe-Ni-S system in the range X_S <0.5 along the temperature axis, Geol. Geofiz., 37, 5–15, 1996.

Lee, Y. M. and Nassaralla, C. L.: Minimization of hexavalent chromium in magnesite-chrome refractory, Metall. Mater. Trans. B, 28, 855–859, 1997.

Lepicard, G. and Protas, J.: Etude structurale de l'oxyde double de manganese et decalcium orthorhombique $CaMn_2O_4$ (marokite), B. Soc. Fr. Mineral. Cr., 89, 318–324, 1966.

Ma, C. and Prakapenka, V.: Tschaunerite, IMA 2017-032a, CNMNC Newsletter No. 46, December 2018, page 1188, Eur. J. Mineral., 30, 1181–1189, 2018.

Ma, C., Tschauner, O., Beckett, J. R., Liu, Y., Greenberg, E., and Prakapenka, V. B.: Chenmingite, $FeCr_2O_4$ in the $CaFe_2O_4$-type structure, a shock-induced, high-pressure mineral in the Tissint martian meteorite, Am. Mineral., 104, 1521–1529, https://doi.org/10.2138/am-2019-6999, 2019.

Mao, H., Hillert, M., Selleby, M., and Sundman, B.: Thermodynamic assessment of the CaO-Al_2O_3-SiO_2 system, J. Am. Ceram. Soc., 89, 298–308, https://doi.org/10.1111/j.1551-2916.2005.00698.x, 2006.

Nigmatulina, E. A.: The first finding of aciculite $CaO{\bullet}Fe_2O_3$ in natural and technogenous burned rocks of the Kuznetsk Coal Basin, in: Mineralogy of Technogenesis-2006, PH IMin UrB RAS, Miass, Russia, 107–122, 2006 (in Russian).

Nigmatulina, E. N. and Nigmatulina, E. A.: Pyrogenic iron ores of fossil coal fires of the Kuznetsk coal basin, Zap. Russ. Mineral. Soc., 138, 52–68, 2009 (in Russian).

Pausch, H. and Müller Buschbaum, H. K.: Die Kristallstruktur von α-$CaCr_2O_4$, Z. Anorg. Allg. Chem., 405, 113–118, 1974.

Pouchou, I. L. and Pichoir, F.: "PaP" (phi-rho-z) procedure for improved quantitative microanalysis, in: Microbeam analysis, edited by: Armstrong, I. T., San Francisco Press, San Francisco, USA, 104–106, 1985.

Róg, G., Kozlowska-Róg, A., and Dudek, M.: The standard Gibbs free energy of formation of calcium chromium (III) oxide in the temperature range (1073 to 1273 K), J. Chem. Thermodynam., 39, 275–278, https://doi.org/10.1016/j.jct.2006.07.005, 2007.

Scheldrick, G. M.: Crystal structure refinement with *SHELXL*, Acta Crystallogr., C71, 3–8, https://doi.org/10.1107/S2053229614024218, 2015.

Seryotkin, Y. V., Sokol, E. V., Kokh, S. N., and Sharygin, V. V.: Natural bentorite – Cr^{3+}-derivate of ettringite: Determination of crystal structure, Phys. Chem. Mineral., 46, 553–570, https://doi.org/10.1007/s00269-019-01022-4, 2019.

Shabanova, G. N., Korohodska, A. N., and Deviatova, N. B.: Refinement of the subsolidus structure of the four-component system Fe_2O_3 – CaO – Al_2O_3 – Cr_2O_3, Vopr. Khim. Khim. Tekhnol., 2, 144–149, https://doi.org/10.32434/0321-4095-2019-123-2-144-149, 2019.

Sharygin, V. V.: Mayenite-supergroup minerals from burned dump of the Chelyabinsk Coal Basin, Russ. Geol. Geophys., 56, 1603–1621, https://doi.org/10.1016/j.rgg.2015.10.007, 2015.

Sharygin, V. V.: Orthorhombic $CaCr_2O_4$ in phosphide-bearing gehlenite-rankinite paralava from Hatrurim Basin, Israel: preliminary data, in: Proceedings of 36th International Conference "Magmatism of the Earth and related strategic metal deposits", Saint Petersburg, Russia, 23–26 May 2019, 272–276, 2019.

Sharygin, V. V., Vapnik, Y., Sokol, E. V., Kamenetsky, V. S., and Shagam, R.: Melt inclusions in minerals of schorlomite-rich veins of the Hatrurim Basin, Israel: composition and homogenization temperatures, in: ACROFI I Program with Abstracts, edited by: Ni, P. and Li, Z., Nanjing, China, 189–192, 2006.

Sharygin, V. V., Sokol, E. V., and Vapnik, Y.: Minerals of the pseudobinary perovskite–brownmillerite series from combustion metamorphic larnite rocks of the Hatrurim Formation (Israel), Russ. Geol. Geophys., 49, 709–726, https://doi.org/10.1016/j.rgg.2008.03.001, 2008.

Sharygin, V. V., Britvin, S. N., Murashko, M. N., and Vapnik, Y.: Mineralogy of phosphide-bearing gehlenite-rankinite paralavas, Hatrurim Basin, Israel, in: Proceedings of scientific conference "Mineralogical museums: yesterday, today and tomorrow", Saint Petersburg, Russia, 17–19 September 2019, 188–190, 2019a (in Russian).

Sharygin, V. V., Yakovlev, G. A., Wirth, R., Seryotkin, Y. V., Sokol, E. V., Nigmatulina, E. N., Karmanov, N. S., and Pautov, L. A.: Nataliakulikite, $Ca_4Ti_2(Fe^{3+},Fe^{2+})(Si,Fe^{3+},Al)O_{11}$, a new perovskite-supergroup mineral from Hatrurim Basin, Negev Desert, Israel, Minerals, 9, 700, https://doi.org/10.3390/min9110700, 2019b.

Sharygin, V. V., Britvin, S. N., Kaminsky, F. V., Wirth, R., Nigmatulina, E. N., Yakovlev, G. A., Novoselov, K. A., and Murashko, M. N.: Ellinaite, IMA 2019-091, in: CNMNC Newsletter 53, Eur. J. Mineral., 32, https://doi.org/10.5194/ejm-32-209-2020, 2020.

Shizuya, M., Isobe, M., and Takayama-Muromachi, E.: Structure and properties of the $CaFe_2O_4$-type cobalt oxide $CaCo_2O_4$, J. Solid State Chem., 180, 2550–2557, https://doi.org/10.1016/j.jssc.2007.07.008, 2007.

Sokol, E., Sharygin, V., Kalugin, V., Volkova, N., and Nigmatulina, E.: Fayalite and kirschsteinite solid solutions in melts from burned spoil-heaps, South Urals, Russia,

Eur. J. Mineral., 14, 795–807, https://doi.org/10.1127/0935-1221/2002/0014-0795, 2002.

Sokol, E., Novikov, I., Zateeva, S., Vapnik, Y., Shagam, R., and Kozmenko, O.: Combustion metamorphic rocks as indicators of fossil mud volcanism: New implications for the origin of the Mottled Zone, Dead Sea area, Basin Res., 22, 414–438, https://doi.org/10.1111/j.1365-2117.2010.00462.x, 2010.

Sokol, E. V., Maksimova, N. V., Nigmatulina, E. N., Sharygin, V. V., and Kalugin, V. M.: Combustion Metamorphism, PH SB RAS, Novosibirsk, 284 pp., ISBN 5-7692-0783-3, 2005 (in Russian).

Sokol, E. V., Novikov, I. S., Zateeva, S. N., Sharygin, V. V., and Vapnik, Y.: Pyrometamorphic rocks of the spurrite-merwinite facies as indicators of hydrocarbon discharge zones (the Hatrurim Formation, Israel), Dokl. Earth Sci., 420, 608–614, https://doi.org/10.1134/S1028334X08040181, 2008.

Sokol, E. V., Gaskova, O. L., Kokh, S. N., Kozmenko, O. A., Seryotkin, Y. V., Vapnik, Y., and Murashko, M. N.: Chromatite and its Cr^{3+}- and Cr^{6+}-bearing precursor minerals from the Nabi Musa Mottled Zone complex, Judean Desert, Am. Mineral., 96, 659–674, https://doi.org/10.2138/am.2011.3487, 2011.

Sokol, E. V., Kozmenko, O. A., Kokh, S. N., and Vapnik, Y.: Gas reservoirs in the Dead Sea area: Evidence from chemistry of combustion metamorphic rocks in Nabi Musa fossil mud volcano, Russ. Geol. Geophys., 53, 745–762, https://doi.org/10.1016/j.rgg.2012.06.003, 2012.

Sokol, E. V., Gaskova, O. L., Kozmenko, O. A., Kokh, S. N., Vapnik, E. A., Novikova, S. A., and Nigmatulina, E. N.: Clastic dikes of the Hatrurim basin (western flank of the Dead Sea) as natural analogues of alkaline concretes: Mineralogy, solution chemistry, and durability, Dokl. Earth Sci., 459, 1436–1441, https://doi.org/10.1134/S1028334X14100122, 2014a.

Sokol, E. V., Kokh, S. N., Vapnik, Y., Thiery, V., and Korzhova, S. A.: Natural analogs of belite sulfoaluminate cement clinkers from Negev Desert, Israel, Am. Mineral., 99, 1471–1487, https://doi.org/10.2138/am.2014.4704, 2014b.

Sokol, E. V., Seryotkin, Y. V., Kokh, S. N., Vapnik, Y., Nigmatulina, E. N.; Goryainov, S. V., Belogub, E. V., and Sharygin, V. V.: Flamite $(Ca,Na,K)_2(Si,P)O_4$, a new mineral from the ultrahigh-temperature combustion metamorphic rocks, Hatrurim Basin, Negev Desert, Israel, Mineral. Mag., 79, 583–596, https://doi.org/10.1180/minmag.2015.079.3.05, 2015.

Sokol, E. V., Kokh, S. N., Khoury, H. N., Seryotkin, Y. V., Goryainov, S. V., Novikova, S. A., and Sokol, I. A.: Natural analogue approaches to prediction of long-term behaviour of Ca_2UO_5•2-3H_2O X-phase: Case study from Tulul Al Hammam site, Jordan, Arab. J. Geosci., 10, 512, https://doi.org/10.1007/s12517-017-3305-5, 2017.

Sokol, E. V., Kokh, S. N., Sharygin, V. V., Danilovsky, V. A., Seryotkin, Y. V., Liferovich, R., Deviatiiarova, A. S., Nigmatulina, E. N., and Karmanov, N. S.: Mineralogical diversity of Ca_2SiO_4-bearing combustion metamorphic rocks in the Hatrurim Basin: Implications for storage and partitioning of elements in oil shale clinkering, Minerals, 9, 465, https://doi.org/10.3390/min9080465, 2019a.

Sokol, E. V., Polyansky, O. P., Semenov, A. N., Reverdatto, V. V., Kokh, S. N., Devyatiyarova, A. S., Kolobov, V. Y., Khvorov, P. V., and Babichev, A. V.: High-grade contact metamorphism in the Kochumdek River valley (Podkamennaya Tunguska basin, East Siberia): Evidence for magma flow, Russ. Geol. Geophys., 60, 386–399, https://doi.org/10.15372/GiG2019088, 2019b.

Sokol, E. V., Kokh, S. N., Seryotkin, Y. V., Deviatiiarova, A. S., Goryainov, S. V., Sharygin, V. V., Khoury, H. N., Karmanov, N. S., Danilovsky, V. A., and Artemyev D. A.: Ultrahigh-temperature sphalerite from Zn-Cd-Se-rich combustion metamorphic marbles, Daba Complex, Central Jordan: paragenesis, chemistry, and structure, Minerals, 10, 822, https://doi.org/10.3390/min10090822, 2020.

Stoe & Cie: X-AREA (Version 1.35) and X-RED32 (Version 1.31), Stoe & Cie GmbH, Darmstadt, Germany, 2006.

Toth, S., Lake, B., Kimber, S. A. J., Pieper, O., Reehuis, M., Islam, A. T. M. N., Zaharko, O., Ritter, C., Hill, A. H., Ryll, H., Kiefer, K., Argyriou, D. N., and Williams, A. J.: 120° helical magnetic order in the distorted triangular antiferromagnet α-$CaCr_2O_4$, Phys. Rev. B, 84, 054452, https://doi.org/10.1103/PhysRevB.84.054452, 2011.

Vapnik, Y., Sharygin, V., Sokol, E., and Shagam, R.: Paralavas in a combustion metamorphic complex, Hatrurim Basin, Israel, GSA Rev. Engin. Geol., 18, 133–154, https://doi.org/10.1130/2007.4118(09), 2007.

Walter, M., Bulanova, G., Armstrong, L., Keshav, S., Blundy, J. D., Gudfinnsson, G., Lord, O., Lennie, A., Smith, C., and Gobbo, L.: Primary carbonatite melt from deeply subducted oceanic crust, Nature, 454, 622–625, https://doi.org/10.1038/nature07132, 2008.

Zateeva, S. N., Sokol, E. V., and Sharygin, V. V.: Specificity of pyrometamorphic minerals of the ellestadite group, Geol. Ore Deposit, 49, 792–805, https://doi.org/10.1134/S1075701507080132, 2007.

Xue, W., Zhai, K., and Zhai, S.: Thermal expansion of ellinaite (β-$CaCr_2O_4$): an in-situ high temperature X-ray diffraction study, Phys. Chem. Mineral., 48, 2, https://doi.org/10.1007/s00269-020-01126-2, 2021.

Zhai, S., Yin, Y., Shieh, S. R. Shan, S., Xue, W., Wang, C.-P., Yang, K., and Higo, Y.: High-pressure X-ray diffraction and Raman spectroscopy of $CaFe_2O_4$-type β-$CaCr_2O_4$, Phys. Chem. Mineral., 43, 307–314, https://doi.org/10.1007/s00269-015-0795-0, 2016.

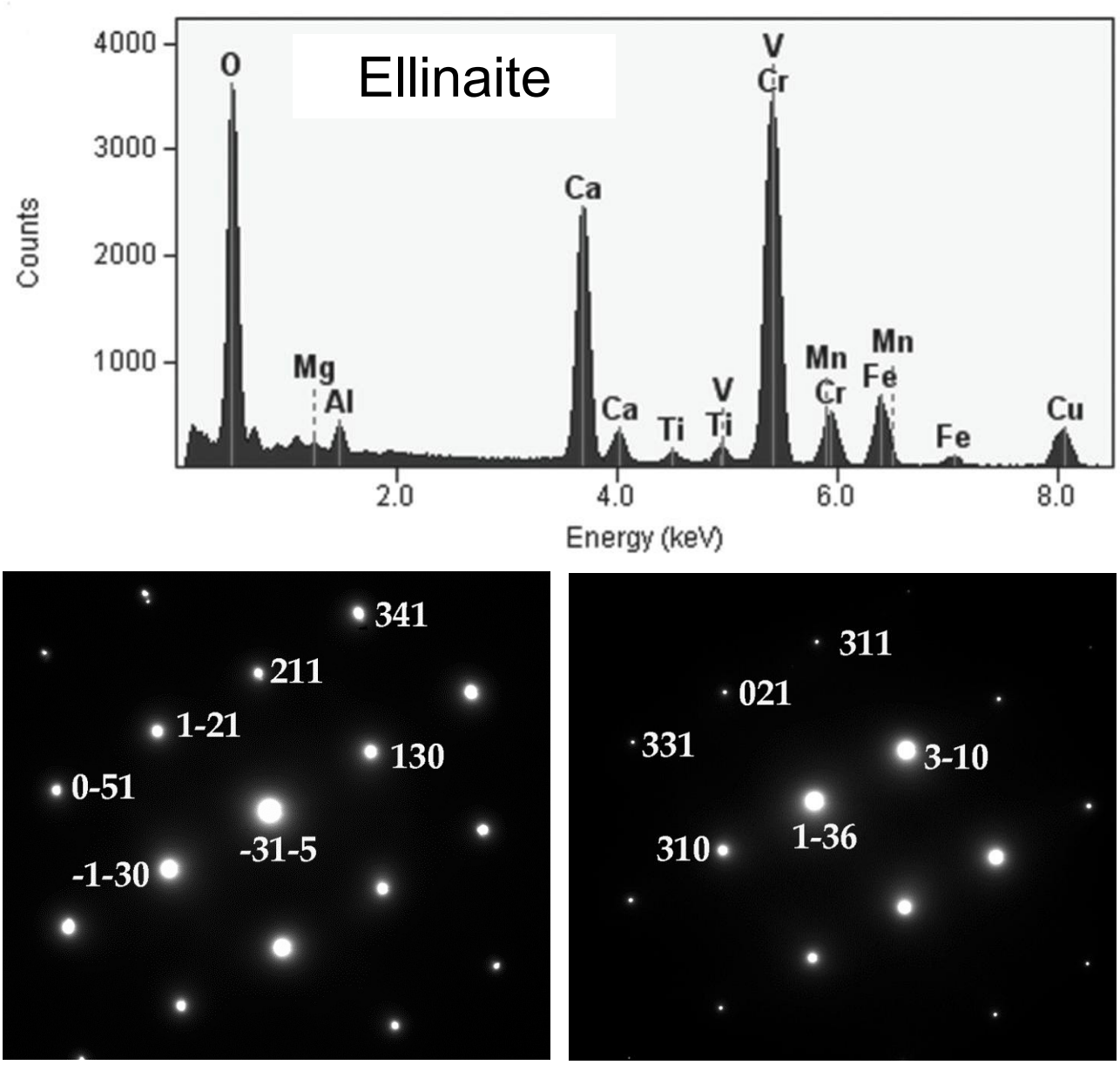

Figure S1. EDX spectrum and indexed electron-diffraction patterns (FFT) from HRTEM images for ellinaite from diamond-hosted inclusion, foil #3601, Brazil. CuK_{α} X-ray intensity comes from the copper grid of the TEM foil rests on (adapted from Kaminsky et al., 2015).

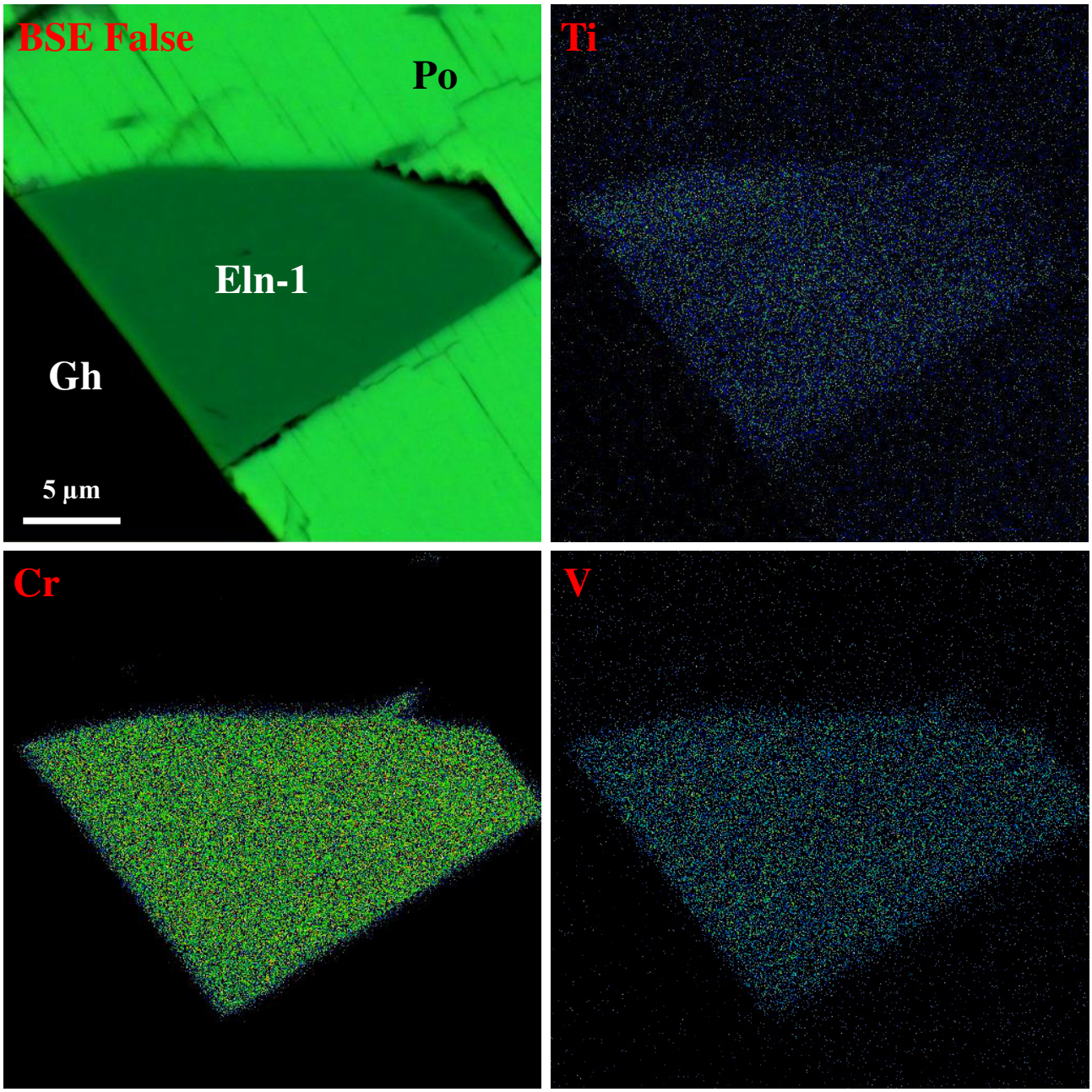

Figure S2. Elemental maps for grain of $CaCr_2O_4$ from Hatrurim Basin, Israel.
Symbols: Eln-1 – ellinaite-1 grain; Po – pyrrhotite; Gh – gehlenite.

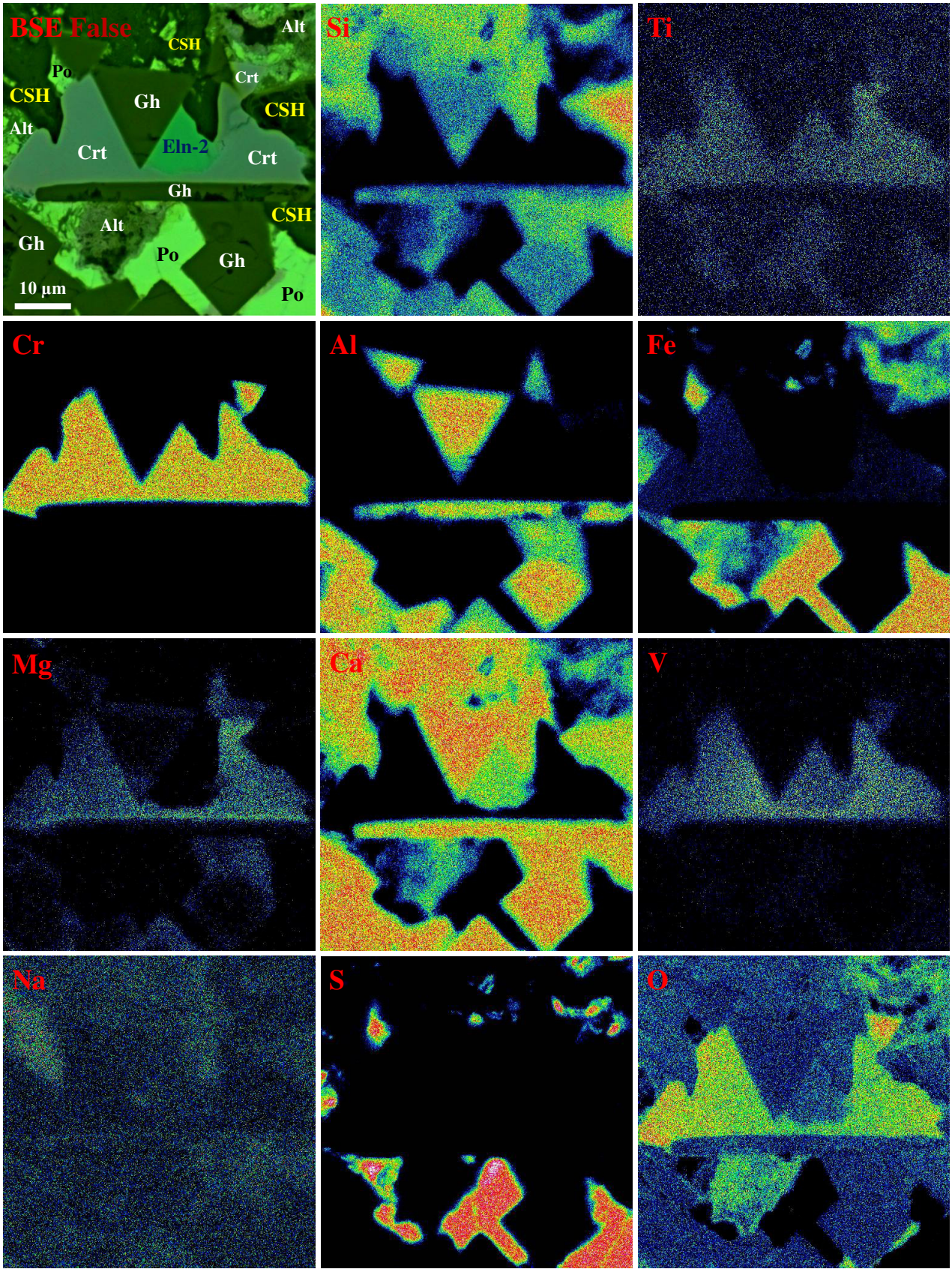

Figure S3. Elemental maps for association with the ellinaite-2 grain from gehlenite-rankinite paralava, Hatrurim Basin, Israel. Symbols: Eln-2 – ellinaite; Po – pyrrhotite; Gh – gehlenite; Crt – chromite-magnesiochromite; CSH – hydrated calcium silicates; Alt – alteration products after pyrrhotite. See Figure 3B for details.

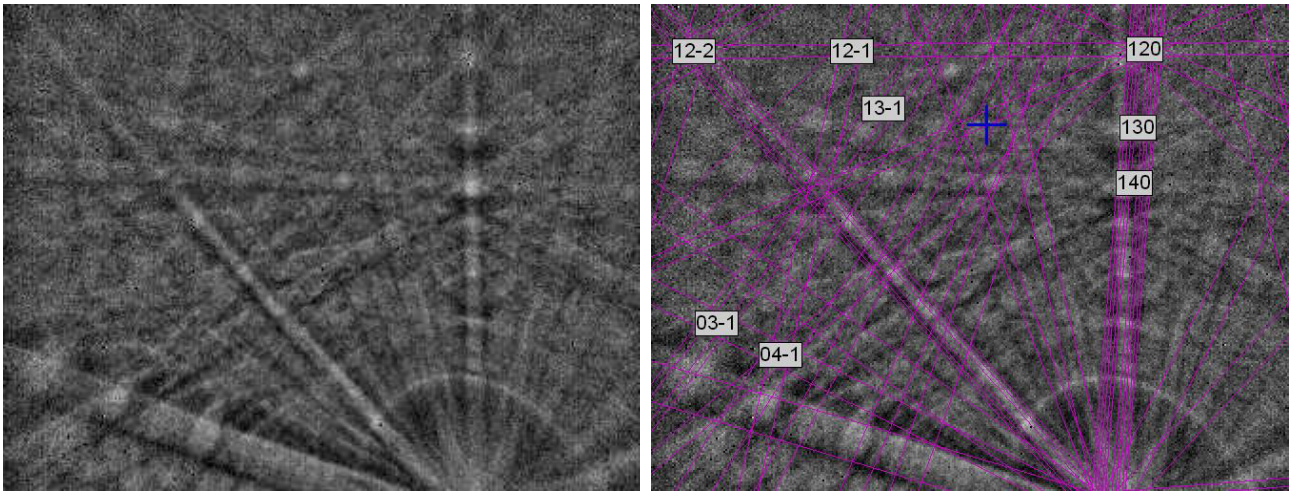

Figure S4. Electron backscattered diffraction (EBSD) pattern and the forced Kikuchi pattern for the ellinaite-1 grain from Hatrurim Basin, Israel (see Figures 2, 3, 6 and S2). The structural data for synthetic β-$CaCr_2O_4$ (Damay *et al.*, 2010) were used for the Kikuchi pattern simulation. Detector distance – 20 mm. The crystal structure of α-$CaCr_2O_4$ (Pauschand and Müller Buschbaum, 1975) was also used for comparison.

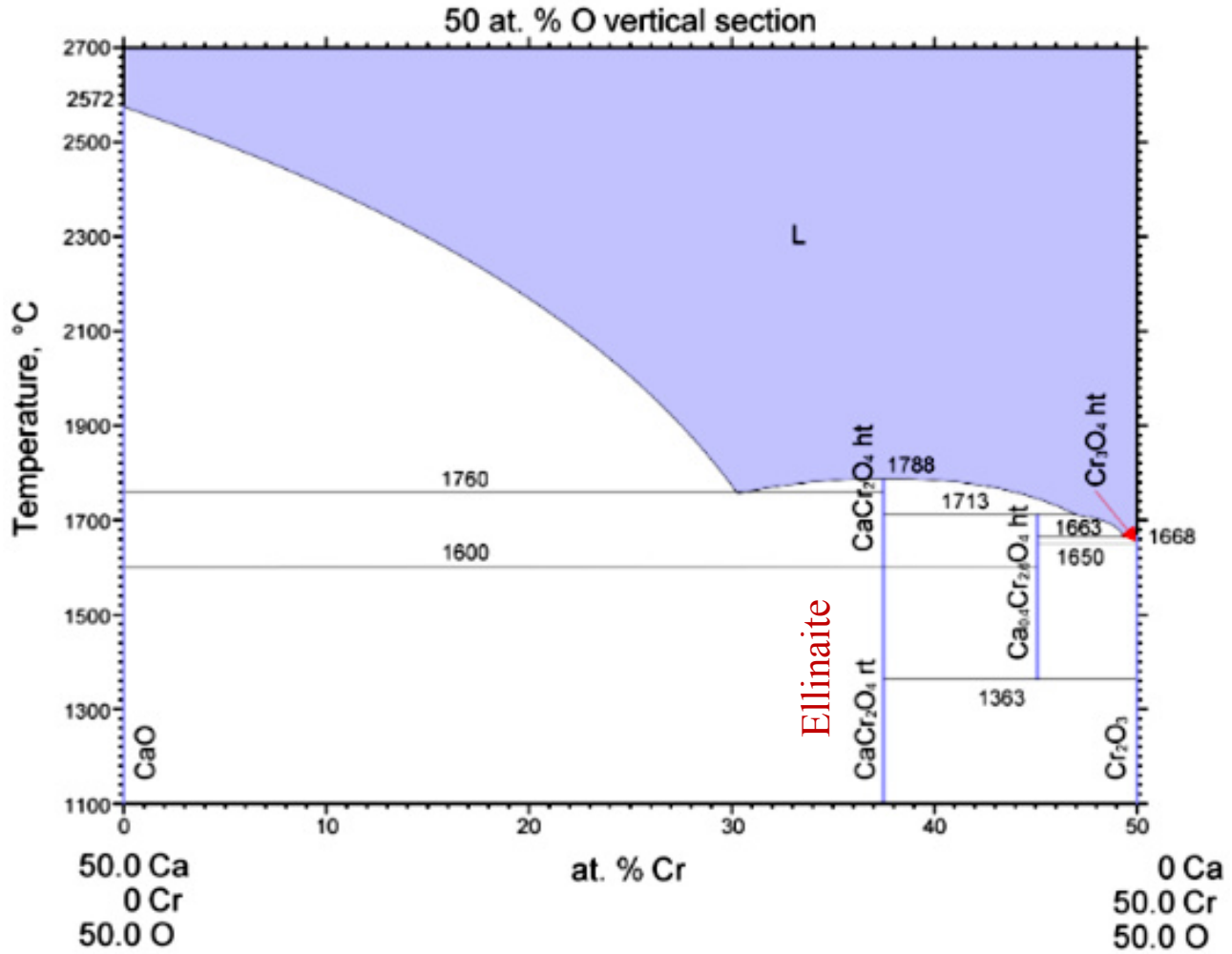

Figure S5. The phase diagram for the system CaO-Cr_2O_3 (adapted from Degterov and Pelton, 1996). The phase transition between α-$CaCr_2O_4$ (ht) and β-$CaCr_2O_4$ (rt, ellinaite) is near 1600°C.

Table S1. List of mineral phases found in the rankinite-gehlenite paralava with ellinaite (sample MP-2013-6), Hatrurim Basin, Israel.

Mineral	Formula	Mineral	Formula
Iron (kamacite)	α-(Fe,Ni)	Goethite	FeO(OH)
Taenite	γ-(Fe,Ni)	Anhydrite	$CaSO_4$
Tetrataenite	FeNi	Baryte	$BaSO_4$
Cohenite	Fe_3C	Fluorapatite	$Ca_5(PO_4)_3F$
Troilite	FeS	Calcite	$CaCO_3$
Pyrrhotite	$Fe_{1-x}S$	Wollastonite	$CaSiO_3$
Pyrite	FeS_2	Larnite	α-Ca_2SiO_4
Pentlandite	$(Ni,Fe)_9S_8$	Flamite	α'$_L$-Ca_2SiO_4 = $(Na,K)Ca_9(SiO_4)_4(PO_4)$
"Gmalimite"	$(K,Ba)_6\square Fe^{2+}{}_{24}S_{27}$	Grossular	$Ca_2Al_3(SiO_4)_3$
Zoharite	$(Ba,K)_6(Fe,Cu,Ni)_{25}S_{27}$	Andradite	$Ca_2Fe_3(SiO_4)_3$
"Ba-Cr-sulfide"	(Ba,Cr)S	"Ca-Fe-silicate"	$Ca_4Fe_2(SiO_4)_3$
"Fe-Ni-As phase"	(Fe,Ni)As	Rankinite	$Ca_3(Si_2O_7)$
"Ni-Fe-As phase"	$(Ni,Fe)_2As$	Gehlenite	$Ca_2Al(AlSiO_7)$
"Ca-Fe-oxysulfide"	$CaFe_3S_2O_5$	Akermanite	$Ca_2Mg(Si_2O_7)$
Wustite	(Fe,Mg)O	Cuspidine	$Ca_4(Si_2O_7)F_2$
Perovskite	$Ca(Ti,Cr,Si,P)O_3$	Thaumasite	$Ca_3(SO_4)[Si(OH)_6](CO_3)$ $12H_2O$
Ellinaite	β-$CaCr_2O_4$	Jennite	$Ca_9(Si_3O_9)_2(OH)_8$ $8H_2O$
Chromite	$(Fe,Mg)Cr_2O_4$	Afwillite	$Ca_3(HSiO_4)_2$ $2H_2O$
Magnesiochromite	$(Mg,Fe)Cr_2O_4$	Tobermorite	$Ca_5Si_6O_{16}(OH)_2$ $4H_2O$
Magnetite	$FeFe_2O_4$	Plombierite	$Ca_5Si_6O_{16}(OH)_2$ $8H_2O$
Hematite	Fe_2O_3	CSH*	calcium silicates hydrated

Identification of mineral phases was based on the EDS, WDS and Raman data (Sharygin, 2019, Sharygin et al., 2019a-b and this work). The names in inverted commas mean poorly identified phases or potentially new mineral species. * Some of Ca-rich secondary minerals were not identified: it mainly concerns to alteration products after larnite-flamite (hydrated calcium silicates) and pyrrhotite. Fe-rich periclase, Mg-rich wustite and poorly identified oxysulfide $Ca_9Fe_{11}S_9O_{13}$ were observed in other samples of the rankinite-gehlenite paralava.

Table S2. Chemical composition (WDS, in wt.%) for essential and minor minerals of the rankinite-gehlenite paralava with ellinaite (sample MP-2013-6), Hatrurim Basin.

Area	EDS spot	Phase	SiO_2	TiO_2	ZrO_2	Cr_2O_3	V_2O_3	Al_2O_3	FeO	MnO	MgO	NiO	CaO	SrO	Na_2O	K_2O	P_2O_5	SO_3	F	Cl	Sum	$O-F_2$	Sum
M6-3	1	Gh	22.78	0.02	0.00	0.00	0.00	33.94	0.29	0.02	0.30	0.00	41.17	0.00	0.07	0.03	0.06	0.00		0.00	98.69	0.00	98.69
M6-3-2	new	Gh-c	25.43	0.04	0.00	0.00	0.00	31.20	0.54	0.00	1.47	0.00	40.43	0.00	0.27	0.08	0.00	0.00		0.00	99.47	0.00	99.47
M6-3-2	new	Gh-Ak-r	31.70	0.05	0.00	0.00	0.00	21.97	0.70	0.00	4.46	0.04	39.83	0.00	0.84	0.18	0.00	0.00		0.00	99.75	0.00	99.75
M6-8	3	Gh	23.12	0.03	0.00	0.00	0.00	34.07	0.23	0.04	0.51	0.00	41.20	0.00	0.05	0.00	0.10	0.00		0.00	99.34	0.00	99.34
M6-n6	1	Gh	22.74	0.00	0.00	0.00	0.00	34.50	0.29	0.00	0.44	0.00	41.08	0.00	0.06	0.00	0.00	0.00		0.00	99.12	0.00	99.12
M6-n7	1	Gh-Ak-r	30.89	0.22	0.00	0.00	0.00	23.01	0.50	0.00	4.73	0.00	39.51	0.00	0.97	0.10	0.00	0.00		0.00	99.93	0.00	99.93
M6-3	2	Ran	41.59	0.08	0.00	0.00	0.00	0.00	0.17	0.00	0.00	0.00	58.35	0.00	0.00	0.00	0.16	0.00		0.00	100.34	0.00	100.34
M6-3-2	16	Ran	41.51	0.08	0.00	0.00	0.00	0.00	0.17	0.00	0.07	0.00	58.25	0.00	0.06	0.00	0.21	0.00		0.00	100.35	0.00	100.35
M6-4		Ran	41.84	0.06	0.00	0.00	0.00	0.00	0.14	0.00	0.08	0.00	58.05	0.00	0.00	0.00	0.20	0.00		0.00	100.38	0.00	100.38
M6-n6	11	Ran	41.38	0.20	0.00	0.00	0.00	0.00	0.15	0.00	0.08	0.00	58.27	0.00	0.00	0.00	0.18	0.00		0.00	100.26	0.00	100.26
M6-8	2	Ran	41.39	0.21	0.00	0.00	0.00	0.00	0.05	0.00	0.07	0.00	58.39	0.00	0.00	0.00	0.19	0.00		0.00	100.30	0.00	100.30
M6-5-new	2	Lar	32.15	0.00	0.00	0.00	0.00	0.32	0.05	0.00	0.02	0.00	63.63	0.00	0.66	0.34	2.77	0.00		0.00	98.94	0.00	98.94
M6-5-new	3	Lar	32.37	0.00	0.00	0.00	0.00	0.00	0.05	0.00	0.02	0.00	63.87	0.00	0.57	0.33	3.02	0.00		0.00	100.23	0.00	100.23
M6-5-new	9	Lar	32.35	0.00	0.00	0.00	0.00	0.00	0.23	0.00	0.02	0.00	63.80	0.00	0.73	0.35	2.91	0.00		0.00	100.39	0.00	100.39
MP6-n7	11	Lar	31.36	0.00	0.00	0.00	0.00	0.15	0.02	0.00	0.02	0.00	62.26	0.00	0.71	0.46	4.61	0.00		0.00	99.59	0.00	99.59
M6-3	3	Flm	28.68	0.00	0.00	0.00	0.00	0.06	0.48	0.00	2.20	0.00	58.23	0.00	0.77	0.37	8.51	0.22		0.16	99.68	0.00	99.68
M6-2	16	Flm	28.94	0.00	0.00	0.00	0.00	0.11	0.20	0.00	0.96	0.00	58.13	0.00	1.04	0.55	7.68	0.34		0.39	98.34	0.00	98.34
M6-2	5	Flm	27.01	0.00	0.00	0.00	0.00	0.00	0.09	0.00	0.16	0.00	59.17	0.00	1.09	0.64	10.34	0.13		0.15	98.77	0.00	98.77
M6-2	8	Cus	32.08	1.26	0.12	0.00	0.00	0.00	0.00	0.00	0.12	0.00	60.40	0.00	0.08	0.00	0.36	0.00	9.74	0.00	104.16	4.10	100.06
M6-2	15	Cus	31.65	1.28	0.06	0.00	0.00	0.00	0.04	0.00	0.10	0.00	60.30	0.00	0.02	0.00	0.72	0.00	9.72	0.00	103.89	4.09	99.80
M6-1	15	Ap	3.14	0.00	0.00	0.00	0.03	0.00	0.37	0.00	0.00	0.00	55.19	0.08	0.00	0.00	39.05	0.10	3.33	0.00	101.28	1.40	99.88
M6-n1	3	Ap-c	3.59	0.00	0.00	0.00	0.00	0.00	0.04	0.00	0.00	0.00	55.10	0.24	0.03	0.00	39.60	0.07	3.59	0.00	102.26	1.51	100.75
M6-n1	4	Ap-r	2.33	0.00	0.00	0.00	0.00	0.00	0.00	0.04	0.00	0.00	55.22	0.23	0.00	0.00	40.53	0.10	3.44	0.00	101.88	1.45	100.43
M6-3-2	9	Ap	3.25	0.00	0.00	0.00	0.00	0.00	0.35	0.00	0.00	0.00	55.41	0.00	0.00	0.00	39.54	0.13	3.03	0.00	101.71	1.28	100.44

Symbols: Gh – gehlenite; Ak – akermanite; Ran – rankinite; Flm – flamite; Cus – cuspidine; Ap – fluorapatite; Si-Prv – Si-rich perovskite; Mg-Crt – magnesiochromite; Crt – chromite; Mgt – magnetite; Wu – wustite; c, r – core, rim of grain. F is determined by EDS.

Table S2 (cont.). Chemical composition (WDS, in wt.%) for essential and minor minerals of the rankinite-gehlenite paralava with ellinaite (sample MP-2013-6), Hatrurim Basin.

Area	EDS spot	Phase	SiO_2	TiO_2	ZrO_2	Cr_2O_3	V_2O_3	Al_2O_3	FeO	MnO	MgO	NiO	CaO	SrO	Na_2O	K_2O	P_2O_5	SO_3	F	Cl	Sum	$O-F_2$	Sum
M6-n1	5	Si-Prv	5.07	44.81	0.00	1.61	1.62	0.79	0.23	0.00	0.46	0.00	42.94	0.00	0.14	0.05	0.74	0.00		0.00	98.46	0.00	98.46
M6-n1	6	Si-Prv	5.76	44.20	0.05	1.62	1.73	0.89	0.18	0.00	0.47	0.00	43.13	0.00	0.15	0.05	0.76	0.00		0.00	99.00	0.00	99.00
M6-n1	7,12	Si-Prv	4.55	45.98	0.00	1.71	1.71	0.90	0.19	0.00	0.40	0.00	42.30	0.09	0.11	0.04	0.41	0.00		0.00	98.39	0.00	98.39
M6-n1	8	Si-Prv	7.22	40.87	0.37	1.95	1.80	1.29	0.26	0.00	0.98	0.00	42.56	0.00	0.09	0.03	0.71	0.00		0.00	98.13	0.00	98.13
M6-n1	9	Si-Prv	6.35	42.06	0.17	1.74	1.63	1.13	0.17	0.03	0.71	0.00	42.85	0.00	0.18	0.03	0.97	0.00		0.00	98.03	0.00	98.03
M6-3	10	Si-Prv	9.74	37.61	0.15	1.71	1.46	1.34	0.26	0.00	1.10	0.00	45.04	0.00	0.38	0.13	1.38	0.00		0.00	100.31	0.00	100.31
M6-3-2	20	Si-Prv	8.49	39.48	0.22	2.21	1.72	1.26	0.22	0.04	1.01	0.00	44.68	0.00	0.23	0.06	0.71	0.00		0.00	100.34	0.00	100.34
M6-2	3	Si-Prv	9.27	38.97	0.00	1.76	1.68	1.21	0.33	0.00	1.04	0.00	44.67	0.00	0.32	0.07	1.50	0.00		0.00	100.82	0.00	100.82
M6-11-2	7,8,9	Si-Prv	8.18	40.30	0.15	2.65	1.79	1.48	0.51	0.00	0.99	0.00	41.42	0.00	0.46	0.04	0.67	0.00		0.00	98.64	0.00	98.64
M6-11-2	2	Si-Prv	10.33	36.03	0.10	2.50	1.92	1.38	0.40	0.00	1.37	0.00	44.37	0.00	0.28	0.12	1.05	0.00		0.00	99.85	0.00	99.85
M6-11-2	3	Si-Prv	8.41	40.21	0.05	2.76	1.89	1.42	0.39	0.00	1.06	0.00	42.20	0.00	0.33	0.04	0.95	0.00		0.00	99.72	0.00	99.72
M6-11-2	4	Si-Prv	8.78	39.05	0.40	2.70	1.93	1.46	0.41	0.00	1.15	0.00	41.94	0.00	0.33	0.05	0.75	0.00		0.00	98.96	0.00	98.96
M6-8	7	Si-Prv	9.27	38.44	0.24	2.45	1.68	1.41	0.18	0.00	1.04	0.00	44.37	0.00	0.30	0.07	1.04	0.00		0.00	100.51	0.00	100.51
M6-8	8	Si-Prv	9.09	38.80	0.14	2.44	1.60	1.43	0.13	0.00	1.23	0.00	44.35	0.00	0.29	0.10	0.95	0.00		0.00	100.54	0.00	100.54
M6-n6	8,7	Mg-Crt	0.17	2.20	0.00	61.95	7.38	1.45	16.30	0.49	9.17	0.00	0.45	0.00	0.00	0.00	0.00	0.00		0.00	99.57	0.00	99.57
M6-n6	3	Mg-Crt	0.20	2.27	0.00	61.32	8.26	1.22	16.56	0.52	9.26	0.00	0.58	0.00	0.00	0.00	0.00	0.00		0.00	100.21	0.00	100.19
M6-n7	5	Mg-Crt	0.24	3.24	0.00	62.29	8.61	0.87	10.61	0.50	13.33	0.00	0.56	0.00	0.00	0.00	0.00	0.00		0.00	100.25	0.00	100.25
M6-11-1	4	Crt	0.00	2.38	0.00	64.29	3.90	1.09	25.17	0.44	3.08	0.00	0.22	0.00	0.00	0.00	0.00	0.00		0.00	100.58	0.00	100.58
M6-11-1	3	Crt	0.00	1.52	0.00	62.21	3.31	3.45	25.23	0.46	3.78	0.00	0.22	0.00	0.00	0.00	0.00	0.00		0.00	100.18	0.00	100.18
MP6-n1-2	13	Wu	0.00	0.00	0.00	0.00	0.00	0.00	99.99	0.00	0.00	0.00	0.26	0.00	0.00	0.00	0.00	0.00		0.00	100.25	0.00	100.25
MP6-n1-2	14	Wu	0.00	0.00	0.00	0.00	0.00	0.00	99.59	0.00	0.68	0.00	0.23	0.00	0.00	0.00	0.00	0.00		0.00	100.50	0.00	100.50
MP6-n1-3	13	Wu	0.00	0.00	0.00	0.00	0.00	0.00	99.87	0.00	0.18	0.00	0.21	0.00	0.00	0.00	0.00	0.00		0.00	100.26	0.00	100.26
M6-11-1	2	Mgt	0.00	0.37	0.00	2.99	0.22	2.22	86.82	0.12	0.53	0.15	0.63	0.00	0.00	0.00	0.00	0.00		0.00	94.05	0.00	94.05

Symbols: Gh – gehlenite; Ak – akermanite; Ran – rankinite; Flm – flamite; Cus – cuspidine; Ap – fluorapatite; Si-Prv – Si-rich perovskite; Mg-Crt – magnesiochromite; Crt – chromite; Mgt – magnetite; Wu – wustite; c, r – core, rim of grain. F is determined by EDS.

Table S3. Variations of chemical composition (in wt.%) for the ellinaite-1 grain from rankinite-gehlenite paralava (sample MP-2013-6), Hatrurim Basin.

Method	Picture	EDS spot	TiO_2 total	Cr_2O_3	V_2O_3	Al_2O_3	FeO	MnO	MgO	CaO	Na_2O	Sum	Sum oxy	Ti^{3+}	Ti^{4+}	Ti_2O_3 calc.	TiO_2 calc.	Sum
	ideal $CaCr_2O_4$			73.05						26.95		100.00	8.000					100.00
EDS	MP-6-4	4	3.52	62.63	6.66	0.60	0.48	0.00		26.11	0.15	100.15	8.091	0.091	0.000	3.17	0.00	99.80
EDS	MP-6-4 2	2	3.65	61.69	7.16	0.77	0.49	0.00		26.11	0.15	100.02	8.094	0.094	0.001	3.26	0.02	99.66
EDS	MP-6-4 2	3	3.54	61.79	7.44	0.74	0.46	0.04		26.16	0.15	100.32	8.092	0.092	0.000	3.19	0.00	99.97
EDS	MP-6-4 2	4	3.62	62.04	7.19	0.89	0.50	0.00		25.92	0.31	100.47	8.084	0.084	0.009	2.94	0.35	100.14
EDS	MP-6-4 2	5	3.22	62.67	6.71	0.60	0.54	0.00		26.12	0.15	100.01	8.081	0.081	0.003	2.79	0.12	99.70
EDS	MP-6-4 2	6	3.44	62.51	6.80	0.67	0.48	0.03		26.12	0.15	100.20	8.089	0.089	0.000	3.08	0.01	99.86
EDS	MP-6-4 2	7	2.87	63.31	6.69	0.66	0.64	0.00		26.08	0.15	100.40	8.074	0.074	0.001	2.56	0.02	100.12
EDS	MP-6-4 2	8	3.49	62.00	7.56	0.72	0.66	0.00		26.15	0.15	100.73	8.090	0.090	0.000	3.13	0.02	100.38
EDS	M6-4-new	3	2.65	63.24	7.55	0.63	0.49	0.00	0.00	26.04	0.26	100.86	8.064	0.064	0.004	2.24	0.16	100.61
EDS	M6-4-new	4	2.75	61.95	7.91	0.64	0.37	0.00	0.00	26.20	0.15	99.97	8.071	0.071	0.001	2.45	0.03	99.70
EDS	M6-4-new	5	3.00	62.55	7.52	0.72	0.45	0.00	0.00	25.80	0.27	100.31	8.077	0.077	0.001	2.67	0.03	100.01
EDS	M6-4-new	6	3.55	62.22	7.11	0.78	0.37	0.00	0.00	25.97	0.23	100.23	8.092	0.092	0.000	3.19	0.01	99.88
EDS	M6-4-new	7	3.62	62.38	6.87	0.66	0.42	0.00	0.00	26.00	0.20	100.15	8.094	0.094	0.000	3.25	0.01	99.79
EDS	M6-4-new	8	3.40	62.74	6.87	0.58	0.55	0.00	0.00	25.97	0.19	100.30	8.088	0.088	0.001	3.04	0.03	99.96
EDS	M6-4-new	9	2.65	63.56	6.68	0.72	0.59	0.00	0.00	26.06	0.22	100.48	8.063	0.063	0.006	2.18	0.23	100.24
EDS	M6-4-new	10	2.50	63.81	6.66	0.66	0.64	0.03	0.00	25.99	0.20	100.49	8.061	0.061	0.003	2.13	0.13	100.25
EDS	M6-4-new	11	2.35	63.63	6.56	0.53	0.75	0.03	0.00	25.87	0.15	99.87	8.059	0.059	0.003	2.02	0.10	99.65
EDS	M6-4-new	12	1.97	63.88	6.55	0.49	0.76	0.01		25.93	0.18	99.77	8.042	0.042	0.009	1.46	0.35	99.61
WDS	M6-4-new	12	2.10	63.97	6.67	0.40	0.88	0.01	0.00	26.13	0.16	100.32	8.042	0.042	0.012	1.47	0.47	100.16
WDS	M6-4-new	10,11	2.31	63.60	6.60	0.40	0.71	0.03	0.00	26.19	0.15	99.99	8.048	0.048	0.012	1.67	0.45	99.81
WDS	M6-4-new	8,9	2.73	63.20	6.94	0.47	0.61	0.00	0.00	26.24	0.19	100.39	8.060	0.060	0.011	2.08	0.42	100.16
WDS	M6-4-new	7	3.07	63.02	6.84	0.51	0.53	0.00	0.02	26.24	0.11	100.34	8.079	0.079	0.000	2.76	0.01	100.03
WDS	M6-4-new	6	3.57	62.19	7.21	0.61	0.53	0.00	0.00	26.33	0.15	100.59	8.088	0.088	0.005	3.05	0.18	100.25
WDS	M6-4-new	5	3.43	62.13	7.43	0.57	0.48	0.04	0.00	26.18	0.18	100.44	8.085	0.085	0.004	2.94	0.16	100.11
WDS	M6-4-new	4	2.69	62.24	7.97	0.57	0.48	0.00	0.00	26.51	0.08	100.54	8.069	0.069	0.001	2.39	0.04	100.27
WDS	M6-4-new	3	2.82	62.03	8.11	0.57	0.45	0.00	0.00	26.47	0.09	100.54	8.073	0.073	0.000	2.53	0.01	100.26
WDS	M6-4-new	new	3.28	61.74	7.82	0.62	0.49	0.00	0.00	26.18	0.14	100.27	8.085	0.085	0.000	2.96	0.00	99.94
WDS	M6-4-new	new	4.08	61.38	7.64	0.66	0.56	0.00	0.00	26.10	0.18	100.60	8.104	0.104	0.001	3.63	0.05	100.19
WDS	M6-4-new	new	4.51	60.72	7.43	0.78	0.65	0.03	0.03	25.96	0.15	100.26	8.117	0.117	0.000	4.05	0.01	99.81
WDS	M6-4-new	new	4.71	60.64	7.45	0.68	0.69	0.03	0.02	25.98	0.14	100.34	8.122	0.122	0.000	4.23	0.01	99.87
WDS	M6-4-new	new	3.86	61.96	7.53	0.63	0.52	0.03	0.00	26.17	0.18	100.89	8.099	0.099	0.001	3.44	0.04	100.51
WDS	M6-4-new	new	3.59	62.46	7.16	0.61	0.63	0.00	0.00	26.10	0.27	100.82	8.080	0.080	0.012	2.81	0.47	100.50
WDS	M6-4-new	new	3.04	61.53	7.66	0.61	0.50	0.00	0.01	26.49	0.14	99.97	8.065	0.065	0.014	2.26	0.53	99.72
WDS	M6-4-new	new	3.30	62.61	7.04	0.67	0.56	0.00	0.00	26.38	0.15	100.71	8.080	0.080	0.006	2.77	0.22	100.40
WDS	M6-4-new	new	3.38	62.13	7.45	0.65	0.47	0.00	0.01	26.38	0.16	100.64	8.082	0.082	0.006	2.85	0.22	100.32
WDS	M6-4-new	new	3.54	62.54	7.12	0.58	0.55	0.00	0.00	26.02	0.19	100.55	8.091	0.091	0.000	3.18	0.01	100.19
WDS	M6-4-new	new	3.20	62.55	6.92	0.54	0.64	0.03	0.00	26.01	0.17	100.06	8.078	0.078	0.005	2.70	0.20	99.75
WDS	M6-4-new	new	2.31	63.60	6.80	0.47	0.81	0.00	0.01	26.16	0.07	100.22	8.059	0.059	0.001	2.04	0.04	100.00
	Ellinaite-1	*n=38*	3.19	62.50	7.17	0.62	0.56	0.01	0.00	26.13	0.17	100.35	8.079	0.079	0.004	2.75	0.14	100.04
		sd	0.61	0.82	0.44	0.10	0.12	0.01	0.01	0.17	0.05					0.71	0.19	
		min	1.97	60.64	6.55	0.40	0.37	0.00	0.00	25.87	0.07					1.47	0.00	
		max	4.71	63.97	8.11	0.89	0.88	0.04	0.03	26.51	0.31					4.23	0.53	

SiO_2, NiO and SrO are below detection limits (<0.005 wt.%). Formula based on 3 cations and 4 oxygens. Ti_2O_3 and TiO_2 are calculated by charge balance.

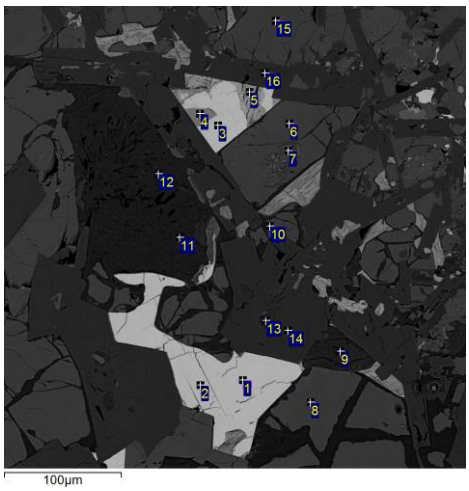

MP-6-4 – BSE image

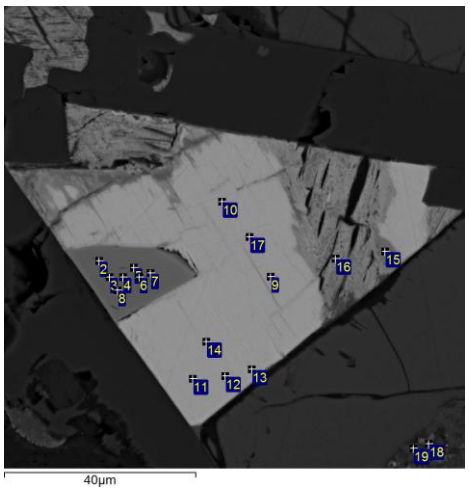

MP-6-4 2 – BSE image

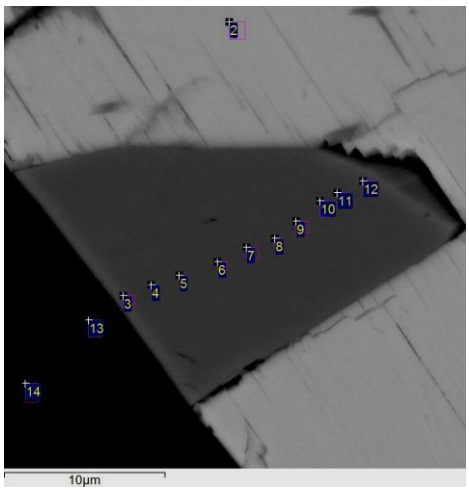

M6-4-new – BSE image

checkCIF/PLATON report

Structure factors have been supplied for datablock(s) Ellinaite

THIS REPORT IS FOR GUIDANCE ONLY. IF USED AS PART OF A REVIEW PROCEDURE FOR PUBLICATION, IT SHOULD NOT REPLACE THE EXPERTISE OF AN EXPERIENCED CRYSTALLOGRAPHIC REFEREE.

No syntax errors found. CIF dictionary Interpreting this report

Datablock: Ellinaite

```
Bond precision:  Cr- O = 0.0050 A        Wavelength=0.71073

Cell:              a=8.868(9)      b=2.885(3)      c=10.355(11)
                   alpha=90        beta=90         gamma=90
Temperature:       296 K
```

	Calculated	Reported
Volume	264.9(5)	264.9(5)
Space group	P n m a	P n m a
Hall group	-P 2ac 2n	?
Moiety formula	Cr4 O8, 2(Ca)	?
Sum formula	Ca2 Cr4 O8	Ca Cr2 O4
Mr	416.16	208.08
Dx,g cm-3	5.218	5.217
Z	2	4
Mu (mm-1)	9.936	9.935
F000	400.0	400.0
F000'	403.63	
h,k,lmax	11,3,13	11,3,13
Nref	351	348
Tmin,Tmax	0.788,0.820	0.273,1.000
Tmin'	0.742	

```
Correction method= # Reported T Limits: Tmin=0.273 Tmax=1.000
AbsCorr = MULTI-SCAN

Data completeness= 0.991          Theta(max)= 26.983

R(reflections)= 0.0588( 312)      wR2(reflections)= 0.1572( 348)

S = 1.105                 Npar= 43
```

The following ALERTS were generated. Each ALERT has the format
test-name_ALERT_alert-type_alert-level.
Click on the hyperlinks for more details of the test.

Alert level C

```
DIFMN02_ALERT_2_C  The minimum difference density is < -0.1*ZMAX*0.75
           _refine_diff_density_min given =     -1.834
           Test value =     -1.800
DIFMN03_ALERT_1_C  The minimum difference density is < -0.1*ZMAX*0.75
           The relevant atom site should be identified.
PLAT088_ALERT_3_C Poor Data / Parameter Ratio .....................       8.09 Note
PLAT098_ALERT_2_C Large Reported Min.  (Negative) Residual Density      -1.83 eA-3
PLAT148_ALERT_3_C s.u. on the      a    - Axis is (Too) Large ....      0.009 Ang.
PLAT148_ALERT_3_C s.u. on the      b    - Axis is (Too) Large ....     0.0030 Ang.
PLAT148_ALERT_3_C s.u. on the      c    - Axis is (Too) Large ....      0.011 Ang.
PLAT250_ALERT_2_C Large U3/U1 Ratio for Average U(i,j) Tensor ....        2.3 Note
PLAT911_ALERT_3_C Missing FCF Refl Between Thmin & STh/L=    0.600          3 Report
PLAT973_ALERT_2_C Check Calcd Positive Resid. Density on       Cr1       1.13 eA-3
PLAT973_ALERT_2_C Check Calcd Positive Resid. Density on       Ca1       1.06 eA-3
PLAT975_ALERT_2_C Check Calcd Resid. Dens.  0.70A   From O1             0.72 eA-3
PLAT976_ALERT_2_C Check Calcd Resid. Dens.  1.03A   From O3            -0.88 eA-3
```

Alert level G

```
PLAT004_ALERT_5_G Polymeric Structure Found with Maximum Dimension          3 Info
PLAT045_ALERT_1_G Calculated and Reported Z Differ by a Factor ...       0.50 Check
PLAT072_ALERT_2_G SHELXL First  Parameter in WGHT  Unusually Large       0.12 Report
PLAT794_ALERT_5_G Tentative Bond Valency for Cr1       (IV)      .       4.12 Info
PLAT794_ALERT_5_G Tentative Bond Valency for Cr2       (IV)      .       3.97 Info
PLAT933_ALERT_2_G Number of OMIT Records in Embedded .res File ...          3 Note
```

---

0 **ALERT level A** = Most likely a serious problem - resolve or explain
0 **ALERT level B** = A potentially serious problem, consider carefully
13 **ALERT level C** = Check. Ensure it is not caused by an omission or oversight
6 **ALERT level G** = General information/check it is not something unexpected

2 ALERT type 1 CIF construction/syntax error, inconsistent or missing data
9 ALERT type 2 Indicator that the structure model may be wrong or deficient
5 ALERT type 3 Indicator that the structure quality may be low
0 ALERT type 4 Improvement, methodology, query or suggestion
3 ALERT type 5 Informative message, check

It is advisable to attempt to resolve as many as possible of the alerts in all categories. Often the minor alerts point to easily fixed oversights, errors and omissions in your CIF or refinement strategy, so attention to these fine details can be worthwhile. In order to resolve some of the more serious problems it may be necessary to carry out additional measurements or structure refinements. However, the purpose of your study may justify the reported deviations and the more serious of these should normally be commented upon in the discussion or experimental section of a paper or in the "special_details" fields of the CIF. checkCIF was carefully designed to identify outliers and unusual parameters, but every test has its limitations and alerts that are not important in a particular case may appear. Conversely, the absence of alerts does not guarantee there are no aspects of the results needing attention. It is up to the individual to critically assess their own results and, if necessary, seek expert advice.

Publication of your CIF in IUCr journals

A basic structural check has been run on your CIF. These basic checks will be run on all CIFs submitted for publication in IUCr journals (*Acta Crystallographica*, *Journal of Applied Crystallography*, *Journal of Synchrotron Radiation*); however, if you intend to submit to *Acta Crystallographica Section C* or *E* or *IUCrData*, you should make sure that full publication checks are run on the final version of your CIF prior to submission.

Publication of your CIF in other journals

Please refer to the *Notes for Authors* of the relevant journal for any special instructions relating to CIF submission.

PLATON version of 13/07/2021; check.def file version of 13/07/2021

Datablock Ellinaite - ellipsoid plot